NBSIR 83-2689

Thermal Radiative Ignition of Liquid Fuels By A CO_2 Laser

U.S. DEPARTMENT OF COMMERCE
National Bureau of Standards
National Engineering Laboratory
Center for Fire Research
Washington, DC 20234

May 1983

Sponsored by:
Air Force Office of Scientific Research
Building 410, Bolling Air Force Base
Washington, DC 20332

NBSIR 83-2689

THERMAL RADIATIVE IGNITION OF LIQUID FUELS BY A CO_2 LASER

Takashi Kashiwagi
Thomas J. Ohlemiller
Takao Kashiwagi
Walter W. Jones

U.S. DEPARTMENT OF COMMERCE
National Bureau of Standards
National Engineering Laboratory
Center for Fire Research
Washington, DC 20234

May 1983

Sponsored by:
Air Force Office of Scientific Research
Building 410, Bolling Air Force Base
Washington, DC 20332

U.S. DEPARTMENT OF COMMERCE, Malcolm Baldrige, *Secretary*
NATIONAL BUREAU OF STANDARDS, Ernest Ambler, *Director*

CONTENTS

LIST OF FIGURES

Page

Abstract

This report summarizes progress in the study of the ignition mechanism of a liquid fuel by a CW CO_2 laser; the period covered is from October 1, 1979 to September 30, 1982. It describes (1) new observations of liquid fuel behavior near and at the liquid/air interface during the laser irradiation with incident fluxes from 260 to 2500 W/cm^2, (2) new time-resolved measurements of temperature and vapor concentration distributions in the gas phase using a newly-developed, high speed, two-wavelength holographic interferometer, and (3) the development of a technique to measure infrared absorption spectra of fuel vapors at elevated temperatures.

High speed photographs reveal the complex behavior of n-decane and 1-decene surfaces immediately after the onset of incident CO_2 laser irradiation. In time sequence one sees the formation of a radial wave, a central surface depression, bubble nucleation/growth/bursting, followed by complex surface motion and further bubbling; typically several (or many) bubble cycles precede ignition. An increase in either the flux or the fuel absorptivity accelerates the whole sequence of events leading to a dominance of bubbling phenomena and decreasing the ignition delay. An increase in oxygen concentration in the surrounding gas phase decreases the distance between the liquid surface and the location of the first appearance of visible emission. However, the distance is independent of peak laser flux within the range studied. Also, oxygen in the gas phase significantly increases the growth rate of the plume shortly after the appearance of fuel vapor at the same peak laser fluxes. Prior to ignition, there are two global chemical reaction stages in the gas phase. The first is a relatively slow process

occurring shortly after the appearance of the plume, at temperatures up to about 400-450°C. The other is a significantly faster process occurring just before ignition at temperatures above 450-500°C.

1. INTRODUCTION

High power lasers are now being developed as tactical weapons. Such lasers pose a threat to aircraft integrity since they can ignite aircraft fuel after fuel tank penetration causing a fire or explosion. However, the ignition of flammable liquids by laser radiation has been studied little and is not well understood. The objective of this study is to obtain a fundamental understanding of the mechanism of the radiative ignition process to aid in the development of future design guidelines for the improvement of aircraft survivability.

This paper is the final progress report on this study for the period from October 1979 to September 1982. The paper consists of three parts; (1) new observation of liquid fuel behavior near and at the liquid/air interface during the laser irradiation, (2) new time-resolved measurement of temperature and vapor concentration distributions in the gas phase during the laser irradiation, and (3) the development of a technique to measure infrared absorption spectra of fuel vapors at elevated temperatures.

2. OBSERVATIONS OF LIQUID FUEL BEHAVIOR AND VAPOR GENERATION DURING CO_2 LASER IRRADIATION

2.1 Background

In previous studies (1,2), the change in ignition delay time for n-decane fuel was measured for various CO_2 laser fluxes, laser incident angles and sizes of the liquid container. It was evident from those studies that several

key processes in the ignition interval required further clarification. One of them, the behavior of the vaporizing liquid fuel and its coupling to the build-up of vapor in the gas phase during the pre-ignition period, is reported in this section.

This section reports various observations from high-speed photographs of n-decane and 1-decene during laser irradiation. The formation, growth and collapse of bubbles in the liquid and the growth of a vapor plume in the gas are described. The primary physical processes in the overall behavior are deduced from these observations by simple qualitative and order of magnitude analyses.

2.2 Experimental Apparatus

A schematic illustration of the experimental apparatus is provided in Figure 1. The Coherent Radiation Model 41 CO_2 laser* emits an approximately 6-7 mm diameter beam (at $1/e^2$ points). Beam power was varied from 195 to 340 watts in the fundamental mode which has a nearly Gaussian power distribution across the beam. The incident flux distribution at the sample surface position was measured prior to experiment by traversing a water-cooled, horizontally-mounted calorimeter with 0.25 mm diameter sensing element. The maximum value of the incident flux measured in this manner is reported as the incident radiant flux in this study.

*In order to adequately describe materials and experimental procedures it is occasionally necessary to identify commercial products by manufacturer's name or label. In no instance does such identification imply endorsement by the National Bureau of Standards nor does it imply that the particular product or equipment is necessarily the best available for that purpose.

A rotating mirror was used as a shutter to provide a step-function onset of irradiance; it then remained open through the ignition event. The onset of laser irradiation, i.e., t = 0, was determined by the signal from a sensitive pyroelectric detector collecting part of the laser beam scattered from a mirror. The signal change turned off a neon lamp inside the high speed camera as an event mark on the film through electronic switching circuitry. However, comparison of this event mark with the onset of events on corresponding picture frames revealed some ambiguity in quantifying each sequence precisely in terms of time from the onset of the laser irradiation. Consequently, timing was frequently referenced to the onset of a surface wave believed to result both from photon pressure and the expansion of the liquid, as described below. Further improvements in procedures to determine the start of the irradiation will be necessary in future studies.

Two high speed cameras (HYCAM) were used simultaneously in each experiment. One of them photographed the liquid surface behavior from the top. This camera was focused on the surface and mounted as shown in Figure 1 so that the illumination seen by this camera was specularly reflected light from an approximately 10 cm high diffusing screen illuminated in turn by a tungsten-halogen lamp. This illumination technique provides graded but high contrast for detecting changes in surface inclination. The second camera photographed either the behavior of fuel vapors in the gas phase made visible by a schlieren system as shown in Figure 1 or the behavior of the liquid beneath the surface by direct photography. In the Schlieren photography, the He-Ne laser beam was cut horizontally from the bottom by a knife edge. Kodak 4X negative film for high speed photography was used for all pictures in this study; most prints were made at enhanced contrast.

The dimensions of the liquid container were 5.5 cm x 7.8 cm by 5.5 cm deep. These dimensions are large enough so as not to affect the ignition delay time (1). Two optical grade quartz flats were used as observation windows in two sides of the container. The container was filled to the top with the liquid fuel. Two liquids, n-decane of 99.6% purity supplied by Fisher Scientific Co. and 1-decene of approximately 99% purity supplied by Sigma Chemical Co., were used as fuel samples. The two fuels were chosen to be as similar as possible in all properties except absorptivity with respect to the CO_2 laser radiation; 1-decene has a substantially higher effective absorptivity (approximately 50 cm^{-1} vs. 16 cm^{-1}) (2) in the liquid and probably also in the vapor. No special precautions such as degassing and further filtering of particulates were taken to assure the absence of potential nuclei in the fuels. In nearly all tests the bulk of the fuels was clean enough to exhibit practically no scattering of the He/Ne laser light used for the Schlieren photography. On the other hand, no precautions were taken to prevent room air dust particles, that could serve as bubble nuclei, from falling on the top surface of the liquids during a test.

Ignition was defined by the first light emission detected by a photomultiplier (maximum sensitivity at wavelength 340 nm), the output of which was recorded by an oscillographic recorder with maximum resolution of $\pm$ 1 msec. At the onset of flaming, a step-function-like output of the photomultiplier was obtained. This provided a well defined measurement of the time of ignition.

2.3 Results and Discussion

2.3.1 Range of Laser Flux

In the authors' previous study using decane (1,2), the range of laser fluxes was from 900 to 4000 W/cm^2 and ignition delay time was in the range of 0.06 ~ 1.0 sec. Since the objective of the present study is detailed observation of behavior of the liquid and of vapor build-up in the gas phase, low laser fluxes in the range of 350 - 950 W/cm^2 were used to make the behavior slow enough to be more easily observed. Also, decene was added as a second liquid fuel to examine the effect of absorption coefficient on the overall behavior. With the present conditions, ignition delay times of decane are in the range of 0.35 ~ 1.0 sec and those of decene, 0.040 ~ 0.085 sec.

2.3.2 Parametric Study of Phenomena

Three parameters, laser flux, incident laser angle with respect to the liquid surface and absorption coefficient of the liquid, were selected in this study. Top view and side view pictures were taken with various combinations of these parameters. Typical examples are shown in this paper. Pictures of decane are shown in Figure 2 for an incident laser flux of 740 W/cm^2 and in Figure 3a and 3b for 410 W/cm^2. The dark band in the side view pictures is due to the liquid meniscus at the window of the container. Surface behavior as seen from above and formation of the vapor cloud in the gas phase as seen from the side are shown for decane with an incident laser angle of 30^o. In Figure 2, the top view pictures and side view Schlieren pictures are shown side by side in correlated time sequence. The left columns of pictures are of

the top view and the right columns are of the side view. For the low laser flux case, top view pictures are shown in Figure 3a and side view Schlieren pictures in Figure 3b. In Figures 3a and 3b, the correlation between the top view pictures and the side view Schlieren pictures is not well established due to the lack of a precise determination of the time when the laser starts to irradiate the decane surface, as described in the previous section (and differences in camera framing rates, as well). The top view pictures in both figures indicate the formation of a faint ring-shape wave motion moving slowly outward radially. As time increases after the laser irradiation begins, the shape of the ring becomes clearer; the center part of the ring is concave. With further increase in time, the top view pictures show a further surface depression at the center of the ring. This further depression is circular and its diameter is about the same as that of the incident laser beam. At the same time, the pictures at low flux indicate the development of small scale complex wave motions between the area of the further depression and the ring. In Figure 3b, side view Schlieren pictures show the formation and growth of a plume-like cloud of decane vapor; the plume appears stable and shows no turbulent eddies. Decane, with its high molecular weight (142), is heavier than the surrounding air despite its elevated temperature (boiling point 174^{o}C). The formation and the initial growth of the vapor plume is thus due to the momentum implicit in the jet-like, rapid vaporization of decane instead of to buoyancy. Therefore, it is probable that the further central surface depression and the subsequent small wavy motions are caused by this momentum (see Section 2.4). In Figure 2, side view Schlieren pictures corresponding to the appearance of the further central depression do not show any plume-like cloud. (Note that it has much less time to move up from the surface.) This is probably due to a low sensitivity setting of the Schlieren

system for Figure 2. Further discussion of this early sequence of events is given in Section 2.4.

In Figure 2, shortly after the appearance of the further central surface depression, a black circle appears in the center of the ring. A similar black circle also appears much later in Figure 3a. The corresponding side view Schlieren picture in Figure 2 indicates a sudden release of decane vapor into the gas phase. The black circle becomes larger with time and the vapor cloud of decane becomes more extensive and turbulent. Side view direct close-up pictures of decane near the surface, shown in Figure 4, indicate extremely rapid growth of a bubble (its diameter is approximately 3 mm) beneath the surface. These pictures were taken with different conditions from those of Figures 2 and 3; they are for decane, a laser incident angle of 30^{o} from right to left and a laser flux of about 2600 W/cm^2. Some properly lighted sequences of top photos clearly show that even at much lower fluxes than this the bubble nucleates, grows and bursts between movie frames (i.e., in $\leq$ 2/3 ms); therefore, the observed black circle in Figures 2 and 3 is an open hole left by the bubble. Shortly after the open hole reaches its maximum size it starts to shrink; this is made complicated by the appearance of a second smaller bubble in the side wall of the first as shown in Figure 4 (a high flux phenomenon; see Section 4). Pictures in the middle of the fourth column of this figure show many small bubbles a few mm beneath the surface. This phenomenon may be due to entrained bubbles caused by the bursting of the first bubble (3,4). The decane surface contour becomes very complex and, except at low fluxes, a second bubble forms before these complex motions damp out. Thus the cycle of formation and collapse of a bubble sandwiched between periods of no bubble is repeated; however, the frequency of bubbling is not exactly regular. The top

view pictures in Figure 2 and Figure 3a indicate the formation and radial outward movement of waves initially generated by the surface depression (see Section 2.4) and later further enhanced by rapid bubble formation/collapse and the associated violent vaporization process. These waves interact so that the surface structure becomes extremely complex as shown in the last columns of Figure 2. At the same time, the side view Schlieren pictures indicate violent vaporization, with decane vapor and liquid decane droplets being thrown in all directions.

Gas phase ignition generally occurs during this complex behavior in the liquid and gas phase. The onset of ignition is controlled by the amount of vapor, the degree of mixing of vapor with air, and the amount of absorption of the laser energy by the vapor. This is illustrated in Figure 5 which shows the location of the first appearance of flame with respect to the irradiated area. In this figure, a side view of the decane surface is seen through the window; the surface is the broad horizontal line across each frame (broadened by the meniscus at the window). The upper part of each frame shows the gas phase; the lower part is liquid decane. The incident laser beam comes from left to right at an angle of 30 degrees with respect to the surface. The small white area of flame that first appears in the bottom of the second column of frames is clearly seen to be in the gas phase about 1 cm above the surface and about 2 cm to the left of the irradiated area (indicated by the bubble on the right side of the pictures). The flame spreads upward from the point of its first appearance, presumably assisted by buoyancy, and then spreads toward the irradiated area of the decane surface along the laser beam.

The observed effects of three parameters, laser flux, incident laser angle and the value of absorption coefficient of the liquid, on the behavior of the liquid surface, bubble formation and vaporization are summarized in Table 1. All information except ignition delay times was obtained from a total of twenty eight separate movies. Since the onset of the laser irradiation is not precisely defined in these pictures and also since some of the phenomena are not sharply visible in some movies, values listed in this table may vary $\pm$ 2 ~ 3 msec.

2.3.3 Laser Flux

Higher laser flux shortens the time to the first appearance of the central surface depression associated with the momentum of the stable, non-turbulent vaporization plume and to the appearance of the first bubble. This is clearly demonstrated by comparison of pictures shown in Figures 2 and 3. The frequency of the bubble formation/collapse cycle tends to increase with increases in laser flux. It also appears qualitatively that the laser flux does not have a significant effect on the size of the bubbles. The pictures show that higher laser flux causes the behavior of the liquid surface to become complex earlier and vaporization tends to become more vigorous.

2.3.4 Laser Incident Angle

Top and side view pictures show that the qualitative behavior of the liquid phase at incident laser angles of 30 and 90 degrees does not differ significantly regardless of total laser power level. Any differences are caused mainly by the change in the laser flux due to the change in the

irradiated area with the incident angle. One noticeable difference between the two angles occurs at high fluxes after the first bubble bursts but before the hole it leaves has collapsed. As was noted previously, in such high flux cases a second bubble can start to form in the wall of the hole left by the first bubble and this complicates the collapse of the first. As shown in Figure 4, the left side of the original bubble hole develops a bulge with the incident laser angle of 30 degrees from right to left. At 90 degrees, the bottom part of the original bubble hole shows this bulge.

Since ignition occurs at the location where the incident laser beam interacts with the appropriate mixture of fuel vapor and air, the location of the first appearance of the flame is expected to change with the incident laser angle. However, this idea is not supported by the fact that, once bubbling starts, fuel vapor is thrown into the gas phase over almost the entire hemisphere by the violent vaporization process and not into a specific direction dependent on the incident laser angle.

2.3.5 Absorption Coefficient of Liquid

The effect of the value of the laser absorption coefficient of the liquid on liquid behavior during the ignition period and also on the overall ignition delay was studied by a comparison of high speed pictures and the measured ignition delay time with decane and decene. The value of the absorption coefficient of decane with respect to the CO_2 laser is 16 cm^{-1} (2) and that of decene is about 50 cm^{-1} (5). Since the only difference between the two molecules is one carbon-carbon double bond at the end of the carbon backbone for decene instead of all carbon-carbon single bonds for decane, the physical and

chemical characteristics of the two liquids are close to each other; the normal boiling temperature of decane is 174.1°C versus 170.5°C for decene (6), the difference in molecular weight is two; thermal properties are close to each other.* Oxidation characteristics are expected to be quite similar, judging from the analogous pair, pentane and pentene. Flammability limits for pentane are 1.4 - 7.8% fuel in air; for pentene they are 1.65 - 7.7% fuel in air (7). Therefore, the difference between the two liquids for this study is mainly the difference in the value of absorption coefficient. Also, it is expected that a similar difference in absorption coefficient applies to vapors from the two liquids.

Top view pictures of decene during the ignition period are shown in Figure 6. The sequence of phenomena, i.e., circular wave motion, the central depression, bubble formation and complicated surface motion, is virtually the same as that of decane as seen in Figures 2 and 3. The distinctive difference between pictures with decene and decane is the generally shorter time scale of events with decene compared to that of decane. This is also indicated in Table 1 in a comparison of various times for the same experimental conditions. It is interesting to note that the times to the appearance of the central depression and to the appearance of the first bubble for decene can be a factor of two to four shorter than those for decane. There are exceptions;

*The heat capacities of n-decane are 314.8 and 234.8 J/mole °C for the liquid and gas, respectively. Comparable values for 1-decene are 300.6 and 224.0 J/mole °C (6). The heat of vaporization of n-decane is 45.6 kJ/mole, whereas the value for 1-decene is 42.7 kJ/mole. The combined "endothermicity" of the heat of vaporization and sensible heat to reach the boiling point for decene is less than 10% below that for decane. However, the difference in absorption coefficients at 10.6 μm, which indicates the difference in the depth of heating by the laser, is over 300%. Therefore, the difference between decane and decene with regard to the vaporization process is mainly a difference in the value of radiation absorption coefficient.

for example, the times to appearance of the first bubble at a laser peak flux of 730 W/cm^2 are comparable for both liquids. The reasons for the few discrepancies of this nature are unclear. Ignition delay times for decene are at least one order of magnitude shorter than those for decane. These trends indicate that the differences in absorption coefficient between the liquids and the vapors can both have a major effect on ignition delay time.

Other differences between the two liquids are the size of the bubbles and the bubble frequency. Bubbles for decene tend to be smaller than those for decane as shown in Table 1, although the quantitative difference needs further definition. Also, bubble frequency for decene tends to be higher than that for decane under the same experimental conditions.

2.4 Sequence of Phenomena and Underlying Processes

2.4.1 Idealized Sequence

Figure 7 shows a series of sketches, in cross-section, of what are believed to be the major steps in the radiation-induced vaporization process. The starting condition, for the first bubble only, is a quiescent liquid at uniform temperature (room temperature). Recall that the incident beam profile is roughly Gaussian and therefore is strongly peaked in the center.

In the second sketch of Figure 7, two changes are apparent. A wave is spreading outward radially from the locus of the beam center and the temperature for some depth below the surface has increased. The expected

depth of the thermal wave will be examined more closely below. It is probable that the initial radial surface wave is due at least in part to photon pressure that suddenly exerts a sustained force on the surface. The static depth of a depression in the liquid surface induced by photon pressure is calculated by equating the static liquid head to the rate of momentum loss of the photons; the result is

$$h_p = (Q_L/c\rho_L g) \qquad (1)$$

where Q_L is the photon energy flux, c is the speed of light, g is the acceleration due to gravity and ρ_L is the liquid density. For a peak radiant flux of the order of 1000 W/cm^2 (high end of current tests), the value of h_p is about 5 micrometers. As a static depression extending smoothly over the beam diameter, this would probably not be visible, even with the rather high contrast specular surface lighting used here. However, we have a dynamic situation here in which we view the surface response to the sudden onset of a force; this produces a wave whose steep sides contribute to its visibility. An additional contribution to this early wave may come from the transient volumetric expansion of the liquid as it heats. Decane expands about 10% in heating up 100^oC; this would cause a static surface height increase of about 10% of the radiation absorption depth over the heating time and a radial outward displacement over the same interval of about 10% of the beam diameter. This may be more visible than the direct photon pressure effect; at least the static height would be greater but the dynamic situation is unclear. The identification of the wave with these early effects is important because, as was noted, the wave onset has been used as a zero time reference in several tests.

In the third sketch of Figure 7, the surface has reached a sufficient temperature for vaporization to become appreciable. This vapor flux is visible as the stable, non-turbulent plume in some of the Schlieren photographs (e.g., Fig. 3b). This vapor absorbs some of the incoming radiation as will be discussed below. If the speed of this plume is sufficient, the reaction force against the surface can cause a further depression. Balancing the static and dynamic heads gives, for this surface depression h_R,

$$h_R = \frac{\rho v_p^2}{2\rho_L g} \qquad (2)$$

For an upward vapor plume speed, v_p, of 75 cm/sec (roughly that obtained from Fig. 3b) and plume density, ρ, taken as that of decane vapor at its boiling point, one finds h_R is about 150 microns. A central depression is frequently visible in the top surface photographs for varying periods before the first bubble appears.

In cases where this depression (plus that due to photon pressure) persists for an extended period (tens of milliseconds) prior to bubble formation, it appears that some instability exists that causes small wavelength surface waves to grow in amplitude especially around the periphery of the depression. This may be a result of some coupling between wave-induced fluid motion, the vapor flux (which causes the waves) and the highly non-uniform radiant flux profile on the liquid surface.

In the fourth sketch of Figure 7, the near-surface layer of the liquid has achieved appreciable superheating because the preceding vaporization process from the top surface has not been able to remove a sufficient fraction

of the incoming radiant energy. In the next sketch, this superheating results in bubble nucleation. The amount of superheating that occurs prior to nucleation will depend on the radiant flux, absorption coefficient of liquid, and on the purity of the liquid. There are two types of nucleation, homogeneous and heterogeneous, the latter caused by impurities or solid particulates in the liquid. In the absence of heterogeneous nucleation, the liquid can be heated to near the superheat limit which is typically constrained by the kinetics of homogeneous bubble nucleation and growth (8-10). The value is typically around 0.89 of the critical temperature; for decane this translates to 285°C (11). Since the normal (1 atm) boiling point of decane is 174°C, this means that one can exceed the boiling point by 111°C before achieving homogeneous nucleation. While we have no definitive measure of the actual amount of superheating achieved here before the first bubble nucleates, it is probable that the superheat limit was not approached. Recent optical measurements in the same experimental set-up using a somewhat lower flux (260 W/cm^2) gave a decane vapor temperature of 200°C just above the irradiated surface (with no visible bubble nucleation); this implies a superheat of 25°C or less for this flux (the vapors absorb the laser radiation after they emerge from the surface and therefore continue to heat) although the sub-surface liquid that did not vaporize in this case could have gotten hotter. The higher fluxes of this work present the potential for greater superheating but it is doubtful that we had the necessary absence of heterogeneous nuclei to permit this. For example, one can estimate that particles slightly too small to make their presence known by scattering of the He/Ne laser light can still nucleate bubbles in decane with about 25°C of superheating. Furthermore, we may have had larger particles settled into the top surface of the liquid; the surface was not protected from room dust which was visibly present in the air by

scattering of the He/Ne light. Finally we note that dissolved gases, which we took no precaution to remove, could also promote nucleation (homogeneous) before the superheat limit is approached (12,13). Various heterogeneous nuclei do tend to initiate bubbles at temperatures well below those needed for homogeneous nucleation (8). It is interesting to note that the first bubble can produce new nuclei (entrained air bubbles) and lessen the amount of superheating necessary to generate subsequent bubbles (3,4).

The radiant flux range used in this study is at least three orders of magnitude lower than that used to cause optical cavitation (14).

Although the mechanism of nucleation per se has been studied extensively, most studies involved nucleation near the heated solid wall or in a homogeneously heated liquid without a wall (14). There is little information available about nucleation at and near the free liquid surface as encountered in the present study.

The last sketch in Figure 7 indicates the consequence of the superheating: when nucleation finally occurs below the surface, bubble growth occurs with great speed. Most (and perhaps all) of the top surface photographs are consistent with bubble growth and breakage in less than one millisecond. The dynamics of bubble growth have been analyzed in detail for the case where the bubble is immersed in an infinite liquid (15). The growth process here is considerably altered by the proximity to the free surface but one conclusion from that work appears quite pertinent here: the first few milliseconds of bubble growth are heavily influenced by inertial forces. We estimate below that the thickness of the superheated layer is of the order of

100 μm for decane (less for decene). The bubble must originate in this thin layer and, as it expands, it stretches the liquid above it, thinning it considerably. Since this top layer is both thinning rapidly and vaporizing rapidly from both sides while continuing to absorb some of the incoming radiation, it is plausible that it breaks in less than a millisecond. Despite the fact that the bubble breaks quickly, the hole it produces does not disappear with equal speed because of the momentum imparted to the liquid (and the weaker forces now countering the presence of the hole). The material that was above the region of nucleation is tossed up and out, frequently forming droplets that may be tossed several bubble diameters away (and out of the laser beam path). Since much of this material was superheated and its surface area per unit volume is sharply increased, there is an "explosive" release of fuel vapor that is turbulent in nature, spreading more randomly than the preceding stable, non-turbulent vapor plume. The impulsive downward force due to bubble expansion and subsequent vapor release causes a persisting (up to tens of milliseconds) hole or depression in the liquid. This movement stretches, mixes and largely erases the thermal layer previously established in the liquid over a diameter about equal to the maximum size of the bubble-induced hole. This in turn largely terminates the vaporization process because the upper liquid layer is cooled. Collapse of the hole is induced by gravity and surface tension once the outward/downward movement of the liquid is brought to a halt. Since the laser irradiation continues (somewhat diminished by vapor absorption), the stage is set for repetition of the heat-up and bubble initiation/growth/collapse sequence abetted by any bubbles left behind; unfortunately, the initial condition is now considerably more complex.

Repetition of this cycle feeds the gas phase with slow vaporization punctuated by rapid multi-directional vapor emissions. As this vapor builds up in the gas phase it absorbs the laser radiation and heats up. Ultimately it will ignite at some point where the proper combination of temperature plus fuel and oxygen concentration persists for a time sufficient to permit thermal runaway. Achievement of this condition is clearly dependent on the whole history of complex cycles like that just described.

2.4.2 Key Processes in Vapor Generation

In the above section, the complex behavior during the vapor generation process was described. To fully rationalize these observations, it is necessary ultimately to develop models describing vapor generation as an integral part of a predictive model of radiative ignition. However, the observed phenomena are too complex to be modeled in detail. In this section, we attempt to determine the dominant processes describing vapor generation by order of magnitude analysis; this can serve as a guide for future modeling efforts. It is of interest to attempt to assess what thermal processes dominate the heat-up time between bubble bursts. Consider first the period before the first bubble. The relative importance of heat conduction and in-depth radiation absorption is indicated by the ratio of their characteristic lengths.

$$\sqrt{K_L t} \; / \; (1/\alpha_L) = \alpha_L \sqrt{K_L t} \qquad (3)$$

Here t is time, and α_L is the absorptivity of the CO_2 laser radiation in the liquid; recall that it is about 16 cm^{-1} for decane and roughly three times

higher for decene. The thermal diffusivities, K_L, of decane and decene are both about $8 \cdot 10^{-4}$ cm^2/sec (7). Then the above ratio becomes $0.45\ t^{1/2}$ for decane and $1.4\ t^{1/2}$ for decene. In all but one case (Table I), the time to the first bubble was 60 msec or less for decane so that the above ratio is typically less than about 0.1; for decene, first bubble times were 10 to 50 msec depending on radiant flux so the above ratio ranges from 0.14 to 0.3. For the high flux cases which are of primary interest here heat conduction is a minor process compared to in-depth absorption. Since the average time between successive bubbles is generally less than the time to the first bubble, this statement is generally valid at later times as well (each bubble tends to reset the clock to zero). Conduction may be important in dissipating some of the thermal energy that is mixed randomly by bubble growth/collapse. One can show also that radial conduction due to the non-uniform laser flux is unimportant in the high flux cases since the thermal layer is thin compared to the laser beam diameter.

There are two principal sources of convective motion prior to the first bubble buoyant flow and surface tension gradient flow (16). The buoyant flow is a result of the non-one-dimensional heating of the top of the liquid. Here we follow the work of Reference 16 but note that in the present case inertial forces are more significant than viscous forces in balancing the buoyancy force. Consider a radial flow proceeding upward and then outward from the center of the laser beam impact point. From a steady state balance of buoyancy and fluid inertia one gets the following (the steady state balance is an upper limit on the present dynamic case).

$$\rho_L v_B \frac{dv_B}{dx} \simeq \beta_L g \Delta T \qquad (4)$$

This is approximated as follows.

$$\rho_L \frac{v_B^2}{R_L} \simeq \beta_L g \, (T_B - T_\infty) \tag{5}$$

so

$$v_B = \left[\frac{R_L}{\rho_L} \beta_L g \, (T_B - T_\infty) \right]^{1/2} \tag{6}$$

Here v_B is the buoyantly induced upward flow velocity, ρ_L is the liquid density, β_L is the change of liquid density with temperature, and T_B is the liquid boiling point. The use of R_L, the laser beam radius, as the characteristic length in the upward flow is rough so we can only estimate v_B crudely. Inserting typical numbers for decane (about the same as decene) one finds $v_B \simeq 8$ cm/sec. Recall that this is a steady state upper limit so that, roughly the average transient value acting on events over a time scale of $(R_L/v_B) \simeq 40$ msec is about half this or 4 cm/sec. Then only for bubble delay times of the order of 10 msec is this motion small; for delays of the order of 100 msec it is substantial, causing a full replacement of the liquid beneath the beam profile.

Consider next the flow driven by the surface tension gradient that is a consequence of the non-uniform laser beam profile. The steady state balance is now between the surface tension gradient force and the inertia of the radial outward flow. Roughly, for unit volume of liquid undergoing this radial motion, we have

$$\rho_L \frac{v_s^2}{R_L} \simeq \frac{\partial \sigma}{\partial T} \Delta T \quad 2\pi R_L \tag{7}$$

or

$$v_s \simeq \left[\frac{1}{\rho_L} \frac{\partial \sigma}{\partial T} (T_B - T_\infty) \, 2\pi R_L^2 \right]^{1/2} \tag{8}$$

Here $(\partial\sigma/\partial T)$ is the change in surface tension with temperature; the other symbols are the same as before except that v_s is the radial outward flow velocity. Inserting typical values for decane (decene is again similar), one finds the surface tension induced velocity, $v_s \simeq 3$ cm/sec. Again this is the steady state upper limit so, roughly, half this value is that pertinent to our transient heat-up process. Since this flow is in the same direction as the buoyant flow, this result provides a small reinforcement to the previous conclusion that these fluid motions become appreciable on a time scale of about 100 msec and are small perturbations on a 10 msec time scale.

This conclusion is reinforced by the experimental behavior of a piece of foam plastic placed on the liquid surface about 1 cm away from the irradiated area in several early high flux tests. This object was always pushed to the side of the container during a 2-3 seconds laser irradiation but its rate of movement was negligible during the time sequence of interest here.

Again, since the main concern here is high flux, short delay behavior, we can assume for now that the above fluid motions are not significant. Then in the period before the first bubble the dominant energy transport mode is in-depth radiation absorption which follows Beer's law. In this case the governing equation is

$$\rho_L C_L \frac{\partial T}{\partial t} = \alpha_L (1 - r) Q_L e^{-\alpha_L x} \tag{9}$$

with

$$T = T_\infty \quad \text{at} \quad x = \infty$$

and

$$T = T_\infty \quad \text{at} \quad t = 0$$

There α_L is the effective absorptivity (corrected for angle of radiation impingement; note that Q_L and α_L have equal and opposite cosine corrections for incident angle which therefore cancel out), r_L is surface reflectivity (generally about 5%) and C_L is the liquid heat capacity. Equation (9) can be solved using Laplace transformation and the temperature distribution is simply

$$T = T_\infty + \frac{(1 - r_L)}{\rho_L C_L} Q_L \alpha_L t e^{-\alpha_L x} \tag{10}$$

and the surface temperature is

$$T_S = T_\infty + \frac{(1 - r_L)}{\rho_L C_L} Q_L \alpha_L t$$

This temperature distribution and the surface temperature variation hold well only until the surface reaches the boiling point. Beyond this, the surface will tend to be held at the boiling point because nucleation is unnecessary there. For deeper molecules (presumably several mean free paths and beyond) nucleation is necessary to escape from the liquid phase and the continued net energy influx causes superheating. The result is a temperature profile perturbed increasingly from that in Eq. (10) by a downward dip near the surface (Fig. 7). The dip is the net result of in-depth radiation absorption, surface evaporation and conduction of heat from the interior to endothermically vaporizing surface. The depth of the dip grows with increasing heat flux but the thickness of the layer affected by conduction decreases so Eq. (10) is less perturbed for higher fluxes. Using Eq. (10) as a first approximation and assuming a superheat prior to nucleation of 25°C (consistent with the preceding discussion), we can roughly estimate the depth of the superheated layer prior to the first bubble. The result, which will be

more nearly correct for the highest fluxes, is approximately 100 microns for decane; it is about 1/3 of this for decene. This implies that the bubble size will be less for decene by roughly the same factor which is consistent with Table I.

Once the first bubble grows and bursts, we immediately have a new form of convective motion in the liquid. As was noted previously, the initial motion induced by the bubble is largely that of radial expansion but it quickly becomes more complex because of the surface proximity. Some of the Schlieren pictures appear to indicate that the net short term effect of the bubble is to push a segment of the upper thermal layer (about equal in diameter to the bubble in width and one to two diameters deep) down into the cold bulk of the fluid and sometimes to entrain clusters of small bubbles; this is qualitatively consistent with other observations (3,4,15). The speed of the generation of subsequent bubbles depends on the product of flux level and liquid absorptivity (see equation (10)). If the product is high (as in the high flux decene case of Table I), the result, already mentioned, is a second bubble in the bottom (or side) of the hole left by the first, despite any convective/conductive cooling this fluid may have experienced during the growth of the original bubble. The further result is quite complex mixing motion in the liquid that should lead to erratic high frequency bubbles.

If the product $(Q_L \cdot \alpha_L)$ is low (as in the low flux decane case of Table I), the bubble-induced hole will collapse and at least partially mix a layer of the order one to two times its original diameter. The mixing, if total, would fully reset the heating process to zero and another bubble would not follow until a time roughly estimable from Eq. (10) (solved with

$T_S \geq T_{BOIL}$); residual sub-surface convection due to bubble collapse would lengthen the interval. This behavior for the small ($Q_L \cdot \alpha_L$) case would imply a bubble interval comparable to the delay time to the first bubble. This behavior is only roughly what one sees for decane at low fluxes, as indicated by Table I.

These bubble-induced liquid motions complicate the determination of bubble frequency considerably. This frequency is of interest because it is probable that it is half the key to the rate of fuel vaporization; the other half of the key is the amount of fuel vaporized in the bubble growth/burst/collapse sequence (plus any vaporization between bubbles).

For now, we note only that there are three idealized limiting cases of vaporization behavior that facilitate analysis of the gas phase vapor build-up. The first is the purely stable, non-turbulent vaporization case in which a bubble never occurs (or, if it does, the bubble size is small compared to all other characteristic lengths in the problem). The ignition processes observed here begin this way but quickly get more complex. Such relatively simple behavior has been observed with solid fuel ignition by radiation (17,18). Since the plume here is fairly mono-directional its interaction with the laser beam depends strongly on the incident angle of the beam; such behavior has been seen experimentally (1).

The second limiting case is that of very low frequency bubbling as described above for the liquid. To the gas this presents a sequence of widely-spaced vapor pulses that might be approximated by delta functions. Transport in the gas is convective and increasingly multi-directional; the

bursting bubbles generate a non-directional vapor plume and between bursts, the negative buoyancy of heavy fuel vapors forces them down, spreading them out away from the incident beam.

The third limiting case corresponds to high frequency, large bubble bursts as described above for the liquid. To the gas this presents a nearly constant, non-directional vapor source. One would expect a more or less hemispherical envelope of vapor to accumulate over the region where the beam is incident. Since the gradients would be primarily radial, the interaction with the laser beam becomes nearly the same regardless of its incident angle although the location of the first appearance of the flame would change with the incident angle; this trend at high fluxes is also seen experimentally (1).

These limiting cases are more amenable to at least approximate analysis. The general behavior seen in the present experiments tends to fall between the second and third limits described above.

3. RADIATIVE IGNITION MECHANISM OF A LIQUID FUEL USING HIGH SPEED HOLOGRAPHIC INTERFEROMETRY

3.1 Background

In most of the previous experimental studies, ignition delay time was selected and measured as the characteristic feature of radiative ignition. Since the ignition delay time represents an integration of the complex interactions of heat and mass transfer and chemical reactions, this information is not sufficient to clarify the fundamental mechanisms of radiative ignition.

Furthermore, in the case of high intensity radiation (e.g., from lasers) the complicated behavior, such as bubble nucleation and thermal expansion in the superheated layer near the liquid surface, renders the systematic analysis of ignition extremely difficult. In the previous section, a qualitative model of bubble formation, growth and collapse in the liquid was presented together with the coupling of these processes to the build-up of vapor in the gas phase during the ignition period. The onset of runaway gas phase chemical reactions leading to ignition was found to be determined by the local temperature, fuel vapor and oxygen concentration.

Therefore, a holographic two-wavelength interferometer was used for the measurement of distribution of temperature and fuel species concentration. The advantages of this optical method are its non-intrusive nature, the capability of high time resolution and, instead of point by point measurements, information about the whole field can be obtained by the evaluation of interferograms. Since the test chamber is illuminated twice within a short space of time, only the temporal changes caused by the phenomena are measured. This means that high quality windows, lenses and mirrors are not necessary in contrast to conventional interferometric methods, such as Mach-Zehnder and Michelson interferometry. Therefore, the necessary optical arrangements are much cheaper; the experimental setup becomes much more flexible; the time needed for adjustment of the equipment and taking measurements is also greatly reduced.

All interferometric methods measure variations in the refractive index. When the refractive index is changed simultaneously by temperature, species concentration or pressure, a conventional single wavelength interferometer

cannot directly evaluate the obtained interference patterns. In this study, temperature and species concentration change simultaneously. Since the refractive index varies with wavelength, temperature and concentration distribution can be evaluated from two interference patterns at two different wavelengths. This application to the mass and heat transfer processes was first attempted by Ross and El-Wakil (19) using a modified Mach-Zehnder interferometer for the study of the steady state vaporization and combustion of liquid fuels. More recently, Mayinger and Panknin (20,21) made further improvement in this technique using holographic interferometry with two lasers for the study of temperature and species concentration of vaporizing naphthalene in the boundary layer. Although their experiments were steady state, they proved clearly that the technique is feasible and has great potential to study heat and mass transfer processes. Mutoh et al. (18) attempted to measure temperature and fuel vapor concentration distributions in the gas phase during the ignition period of polymethylmethacrylate (PMMA) by CO_2 laser beam irradiation using two-wavelength Mach-Zehnder interferometry. However, published results appear not to have sufficient time resolved sequential and spatially accurate information. To understand the mechanism of radiative ignition, the work by Mutoh et al. (18) is also limited to only air as an environmental gas.

In this study, holographic two-wavelength interferometry is developed to attempt measuring time-dependent sequential distributions of temperature and fuel vapor concentration from the start of the laser irradiation to the onset of ignition. The effect of initial gas phase oxygen on the ignition is also studied by varying the concentration of oxygen. Preliminary results of the measurement and of the effect of oxygen are reported in this paper.

3.2 Experimental Apparatus

The optical set-up of the two-wavelength holographic interferometer is schematically described in Figure 8. The entire set-up except a movie camera is mounted on an airsuspended optical bench to isolate the system from any external vibration. In this study, beams from a He-Ne laser (632.8 nm) and an Ar-ion laser (488 nm) are used as light sources. A temperature controlled etalon was installed in the Ar-ion laser to avoid mode hopping. The two beams are superposed at a cube prism beam-splitter, then this combined beam is split into two. One of them is called the reference beam and the other is called the object beam. Both beams are then expanded to parallel waves by telescopes which consist of a microscope objective and a collimating lens. Pinholes with 10 μm diameter are used for both beams at the focal point of the microscope objective lens to remove any fringes on incoming laser beams due to dust scattering. The object beam passes through the test section, in which will be the temperature and vapor concentration field to be examined, whereas the reference beam passes directly onto the photographic plate and interferes with the object beam to make a hologram. Kodak 649 F glass plate was used for the photographic plates. It may be mentioned that not only the object beam is reconstructed by the reference beam of the same wavelength, but also that a false object wave is obtained. This unwanted wave, however, emerges at a different angle from the hologram and can therefore easily be separated from the original wave.

The unique feature of this experiment is its ability to temporarily record interference patterns generated by two wavelengths of light caused by changes in temperature and fuel vapor concentration resulting from the start

of the CO_2 laser irradiation onto the 1-decene surface up to the event of ignition. The basic procedure for recording these patterns is described as follows. Installing a camera shutter at the exit of the laser, a hologram is taken at the glass plate for each laser beam separately without the CO_2 laser irradiation. A hologram for each wavelength is superposed on the glass plate. The plate is developed in a liquid gate without moving it or developed in a darkroom after removing it. In the latter case, the developed plate must be replaced at the same position precisely as it was during the first exposure. After the plate is developed, both lasers are turned on and the reference beam and object beam again interfere at the hologram. The diffracted wave front from the hologram due to the reference beam can interfere with the object wave front passing through the hologram. When there is no change in the test section, if the hologram plate is slightly tilted, the infinite fringe pattern occurs (22). By controlling the amount of the tilt angle and direction of the tilt, number of fringes and direction of fringes can be adjusted. In this study, typically about 70 to 80 fringes nearly parallel to the sample surface are created in the observation field. With changes in temperature and fuel vapor concentration during the ignition period, interference fringe shifts occur in the field. Since changes in temperature and fuel vapor concentration occur rapidly, changes in the interference fringe pattern for both wavelengths must be recorded simultaneously. As shown in Figure 8, the time-dependent fringe shift of both wavelengths is recorded on 16 mm color movie film (Eastman Ektachrome Video News Film 7239) using a Locam Model 50 high speed movie camera which is a pin-registered, intermittent transport camera. The advantage of using this camera is that the film is stationary as each frame is exposed rather than in motion as in other cameras. Therefore, the fringe pattern taken by this camera is sharper. Although its disadvantage is a

relatively low maximum framing rate of 500 frames/sec, this framing rate is high enough for this study. From this color film, the two interference fringe patterns for wavelengths of 488 nm and 632.8 nm are obtained from each frame using two color filters or interference filters.

A test chamber was constructed to avoid the effect of any air movement in the room on the experiment and also to permit study of the effect of initial oxygen concentration on the distributions of temperature and fuel vapor concentration. Since the holographic technique does not require high optical quality windows commercial PMMA sheet was used to construct the chamber. A NaCℓ window was used on the top of the chamber for the transmission of the CO_2 laser beam into the chamber.

The conversion from the measurement of fringe shift to values of temperature and fuel vapor concentration is well documented in previous publications (19,21,22) and only a brief discussion is given here. If the temperature and fuel concentration distributions can be assumed to be axi-symmetrical around the axis passing through the center of the vertical CO_2 laser beam, the index of refraction n(z, r) for the wavelength of λ can be expressed as follows (22):

$$n_\lambda(z, r) = n_{\lambda o} - \frac{\lambda}{\pi} \int_r^R \frac{(dN/dx)dx}{(x^2 - r^2)^{1/2}} \qquad (11)$$

where $n_{\lambda o}$ is the refractive index for the surrounding environmental gas such as the nitrogen, air (21% O_2) or 40% O_2/60% N_2 used in this study. In cylindrical coordinates (r,z) in the hot fuel vapor plume, z is the height from the liquid surface, r the radial distance from the axis, and x the dummy

path variable of integration, respectively. R is the radius of the hot fuel plume and N_λ is the number of fringe shifts seen in an interferogram. In addition, the following relationship between the refractive index and molar refractivity of the mixed gas (the environmental gas and the fuel vapor) can be obtained from the following expression assuming perfect gas behavior (21).

$$\frac{2}{3}\,\delta_\lambda\,(r,z) = \frac{P}{RT(r,z)}\left\{(M_{f\lambda} - M_{a\lambda})\,C_f(r,z) + M_{a\lambda}\right\} \qquad (12)$$

Here, $\delta_\lambda = n_\lambda - n_{\lambda o}$, $M_{f\lambda}$ and $M_{a\lambda}$ are the molar refractivities of the fuel vapor and environmental gas at the wavelength λ, and C_f is the molar concentration of the fuel vapor. T, P, and **R** denote thermodynamic temperature, pressure and the universal gas constant, respectively. The values of $M_{f\lambda_1}$, $M_{f\lambda_2}$, $M_{a\lambda_1}$, and $M_{a\lambda_2}$, calculated using data from reference 23, are listed in Table 2 for the three environmental gases used in this study.

Table 2.

Molar Refractivity (cm^3/mole)

Wavelength (nm)	488	632.8
1-decene vapor	49.603	48.885
N_2	4.500	4.459
Air	4.413	4.370
40% O_2/60% N_2	4.334	4.289

Equation (11) can be written for two different wavelengths, λ_1 and λ_2. Then, the temperature and 1-decene vapor mole fractions can be expressed as

$$T = \frac{T_o}{1 - \frac{2}{3} T_o RF} \tag{13}$$

$$C_f = \frac{\left(\delta_{\lambda_1} M_{a\lambda_2} - \delta_{\lambda_2} M_{a\lambda_1}\right)}{\left(\delta_{\lambda_2} D_{\lambda_1} - \delta_{\lambda_1} D_{\lambda_2}\right) + \frac{3}{2RT_o}\left(M_{f\lambda_1} M_{a\lambda_2} - M_{f\lambda_2} M_{a\lambda_1}\right)} \tag{14}$$

where $D_{\lambda_i} = M_{f\lambda_i} - M_{a\lambda_i}$ and $\delta_{\lambda_i} = n_{\lambda_i} - n_{\lambda_i o}$

and $$F = \frac{D_{\lambda_1} \delta_{\lambda_2} - D_{\lambda_2} \delta_{\lambda_1}}{M_{f\lambda_2} M_{a\lambda_1} - M_{f\lambda_1} M_{a\lambda_2}}$$

The scheme used for data analysis from a 16 mm movie frame to deduce distributions of temperature and fuel vapor mole fraction is summarized in Figure 9. After the blue and red interferograms are separated by filters, a black and white negative film of 10 x 12.5 cm is made for each wavelength interferogram. The light transmission through the film is measured over the entire frame by a computerized automatic scanning densitometer. The range of the spatial resolution of the densitometer is 25 ~ 200 μm, and the number of digitized transmittance values for each frame is typically 1.5 million points; these are stored on magnetic tape. A typical interferogram reconstructed by the computer is shown in Figure 10, which is exactly the same as the original interferogram except at the top of the plume where a fringe line becomes wider and less clear. In defining the locations of the peaks of the fringes, peaks within one scan are determined by taking the derivative of quadratic profiles fitted to a sequence of data points in an interval which is 40% of the peak transmittance (above the background transmittance value). The search for the

next peak in the same scan is initiated beyond the point at which the last sequence terminated. Once we obtain all possible peaks within a scan, their orders are matched with those from the previous scan. Unmatched peaks are eliminated. A typical result for a computer-generated contour of fringe peaks with 1-decene and blue light is shown in Figure 11. Further improvement in the determination of fringe contour is required to obtain more accurate measurement of fringe shift. This is currently in progress. For this report, the amount of each fringe shift was measured manually from movie frame enlargements projected on a large screen. The accuracy of this fringe measurement technique is at best ± 0.1 fringe because of the difficulty in locating the peak of each fringe. Another difficulty is correcting for the difference between the two wavelengths in the location of the base fringe lines. These factors result in estimated uncertainties in the temperature and fuel vapor concentration measurements of about 5 ~ 10% near the liquid surface, increasing to about 10 ~ 15% at the top of the vapor plume as long as the plume is axisymmetric. Our preliminary work using the automatic scanning densitometer indicates that the order of the accuracy of the fringe shift measurement can be improved. Much more accurate results for temperature and fuel vapor concentration are therefore expected in the near future. The reproducibility of the detailed shape of distributions of temperature and vapor concentration measurements is roughly 10%. The major cause of the scatter is due to two effects: variation of the CO_2 laser power flux distribution and somewhat irregular plume growth shortly after the appearance of vapor. However, this scatter does not change the qualitative conclusions reached here.

3.3 Results and Discussion

3.3.1 Observation from High Speed Motion Pictures

The experiments were carried out at peak CO_2 laser fluxes of 260, 520 and 780 W/cm^2. Three different gas environments, nitrogen, air, and a 40% O_2/60% N_2 mixture, were used to study the effects of oxygen concentration. The effects of incident laser radiant flux and oxygen concentration in the gas phase on the distribution of temperature and vapor concentration and the location of the first appearance of the flame were studied. Typical results are shown in Figure 12. These high speed pictures are the negative prints based on the red laser beam. The liquid surface can be seen at the bottom of each frame. The pictures shown in Figure 12(a), (b) and (c) were taken at the same radiant heat flux of 260 W/cm^2, which is the lowest heat flux used in this experiment. With this flux, the formation and growth of a steadily rising plume-like cloud of decene vapor can be observed in each environment. It is found that the time from the start of the CO_2 laser irradiation to the appearance of vapor is approximately the same ($\approx$40 msec) for the three environmental gases. Subsequently, the plume height grows more rapidly and also becomes wider. With the 40% O_2/60% N_2 environment, visible light emission is observed from the upper part of the plume nearly 120 msec after the start of the laser irradiation. One frame prior to this, rapid expansion of the plume is observed. This causes the upper part of the plume to become fuzzy as shown in Figure 12(b). If ignition is defined as the first appearance of the visible emission, this time period of 120 msec corresponds to the ignition delay time.

In air, the height of the steadily rising vapor plume (about 26 mm) at ignition is taller than that in 40% O_2/60% N_2 (about 18 mm). It is clear that ignition is initiated near the top surface of the plume in an umbrella-shaped zone, although the amount of light emission there is much less than that in 40% O_2/60% N_2. Then the flame propagates downward rapidly through the flammable gas mixture. Note the steep gradient in the interference fringe shifts which can be seen near the top surface of the hot vapor plume for several frames before ignition; this indicates very high temperatures in this region. More quantitative discussion of this will be given later. With nitrogen as the environmental gas, nearly the same behavior as with air can be seen. Of course, there is no ignition because of the absence of oxygen.

With an increase in peak laser flux, the vaporization process becomes more complex, with the formation of bubbles followed by violent throw-off of liquid droplets and vapor from bursting bubbles. This behavior of the liquid surface directly affects the growth of the vapor plume. This complexity is unique to liquid fuels; the plume growth pattern is independent of laser peak flux for a solid fuel (24). At peak laser fluxes of 520 W/cm^2 and 780 W/cm^2, the shape of the vapor plume becomes extremely complicated and non-axisymmetric. Such behavior is shown in Figure 13 for 520 W/cm^2. The initial stage of growth of the vapor plume is random in direction and is controlled by the bubbling of the liquid. A discussion of the formation of bubbles and their characteristics is given in a previous section of this report. After about 60 msec of laser irradiation, the upper part of the vapor cloud forms a reasonably stable plume similar to those in Figure 12 at 260 W/cm^2. Although the lower part of the plume retains an asymmetric and complicated vapor distribution, it appears that the upper part of the plume proceeds to ignition

and the subsequent umbrella-shaped ignition patterns are similar to those in Figure 12. The present approach (which assumes symmetry around the center axis of the plume and the CO_2 laser beam) might allow analysis of the upper part of the plume where the actual ignition event occurs. However, if the entire plume needs to be analyzed, some other approach such as tomography would be required.

The vapor plume shown in Figure 12 is narrower than that from the solid fuel (PMMA) studied previously (24). The molecular weight of MMA vapor is 100 which is less than that of 1-decene vapor (MW 142). The average density of the generated gas mixtures for either 1-decene or MMA at the central, near-surface part of the plume is higher than that of the surrounding air even when the temperature effect is included. This is confirmed by the change in the direction of the fringe shift from the lower part of the plume (upward) to the upper part (downward) as shown in Figure 12. Therefore, in the process of vapor plume growth, the initial plume is formed by the momentum of the vaporization from the surface against its negative buoyancy. It acts like a jet of weak momentum. In jets, the radial spreading rate increases with lower molecular weight of the injected gas and this is why the vapor plume of 1-decene is narrower than that of PMMA.

3.3.2 The Growth of the Vapor Plume and the Location of Ignition

The effects of oxygen concentration in the environmental gas and peak laser flux on the growth of the vapor plume and on the location of ignition are described in this section. The growth of the fuel vapor plume is shown in Figure 14 as a function of oxygen concentration and peak laser flux. The peak

height of the plume was selected as the representative value for examining the growth history. As seen from these figures, the plume growth for 260 W/cm^2 and 520 W/cm^2 is the same, but at 780 W/cm^2, a reverse trend between air and 40% O_2 occurs in the early stage of irradiation. It is not clear why this reverse trend for the oxygen effect occurs, but it may be that the violent bubbling behavior disturbs the consistent growth of the plume at this peak laser flux.

There are three regimes in the growth of the plume as shown in Figure 14. They are: a short early buildup stage (most obvious at the lowest flux), followed by a constant growth regime with nearly constant slope and, finally, a sudden rapid growth regime with increasing slope. The effect of the ambient oxygen concentration on the growth rate of the plume appears clearly in the last two regimes and becomes stronger with increase in oxygen concentration at the same peak laser fluxes. Since the difference in the size of the vapor plume between the nitrogen environment and an oxygen-containing one must be based on gas phase oxidative chemical reactions, the contribution from such gas phase chemical reactions appears much earlier than was previously thought (25). Further discussion about the gas phase chemical reactions will be given in the next section together with the results on temperature and fuel vapor concentration.

The rate of growth of the vapor plume increases with peak laser flux; the average speed of plume growth in the constant growth regime is about 19 cm/sec for 260 W/cm^2, 34 cm/sec for 520 W/cm^2 and 48 cm/sec for 780 W/cm^2 with air. This is expected, because the rate of vaporization of the fuel increases with an increase in peak laser flux. Also the rate of expansion of the gases in

the plume tends to become larger because there is a larger amount of absorption of the CO_2 laser beam by the gases in the plume with higher peak laser flux. However, the above growth rates are roughly 40% smaller than those with PMMA under the same experimental conditions (24).

Other important results shown in Figure 14 are the effects of oxygen concentration and of peak laser flux on the location of ignition. In this work, we have defined ignition as the first measurable emission in the motion picture frames. This location is generally near the top of the vapor plume, and it is reasonable to assume that the height of the vapor plume at ignition is proportional to the distance from the location of ignition to the liquid surface. The difference in the plume height at ignition shown in Figure 14 for various conditions can thus represent the change in the location of ignition. The figure shows that an increase in oxygen concentration lowers the location of ignition toward the surface. Surprisingly, however, an increase in peak laser flux does not change the location of ignition; it remains at about 26 ~ 27 mm above the fuel surface. The first effect is also observed with PMMA, but the distance of ignition from the surface tends to increase with peak laser flux for PMMA (24). We believe that differences in the vaporization process between decene and PMMA and also convective motions in the liquid are responsible for this different trend for the effect of peak laser flux on the location of ignition. Further discussion of the location of ignition will be given in the next section together with the results of temperature and fuel vapor concentration.

3.3.3 Distributions of Temperature and Fuel Vapor Concentration

The temperature and fuel vapor concentrations were calculated using the procedure described in Section 3.2. Values of the refractive indices were evaluated by the onion skin technique (22) for solving Eq. (11). Three typical frames were selected from the movie picture for a flux of 260 W/cm^2 as an example: 120, 140 and 158 msec after the start of the CO_2 laser irradiation. As discussed in the previous section, these values belong to the constant plume growth stage, the middle of the rapid growth stage and just before the ignition, respectively.

The comparison of temperature and fuel vapor concentration distributions between air and nitrogen environments at the three different times after the start of the CO_2 laser irradiation are shown in Figure 15(a), (b) and (c). Figures 15 clearly indicate that the temperature in air is higher than that in nitrogen in each stage and especially in the upper part of the plume. Also, the fuel vapor concentration in air is slightly lower than that in nitrogen. The differences in temperature and fuel vapor concentration between the two environmental gases are the result of chemical oxidation reactions. In the case of 120 msec, the difference in maximum temperature between the two gases reaches nearly $100^{o}C$ near the center of the plume. With the approach to ignition, the temperature of the upper part in the plume increases rapidly in the case of air. These results are consistent with the characteristics of the growth rate of the vapor plume shown in Figure 14. From an examination of Figure 14 and Figure 15(a), (b) and (c), it is reasonable to consider that there are two global regimes of gas phase chemical reactions with air: one is that of slow, rather steady reactions starting at an early stage with a

temperature up to about 400 ~ 450°C corresponding to constant growth of the plume; the other is that of much faster chemical reactions occurring near ignition with the temperature above 450 ~ 500°C, coinciding with rapid growth of the plume.* In the same manner as shown in the authors' previous paper for solid fuels (24), this classification also confirms the important role of chemical reactions and their complexity, similar to the multi-stage chemical reaction regimes prior to ignition reported by Gray, et al. (26). It should be noted, especially, that at 158 msec (just before ignition), the highest temperature region (near 800°C) exists near the top center part of the fuel vapor plume, where the fuel concentration is between 1 and 5%. Since this range of concentration is within the flammability limits of decene (0.8% and 5% at room temperature, as predicted from (27), and wider at elevated temperatures), it is reasonable to expect that runaway chemical reactions will occur in this region. If the visible emission follows the runaway chemical reactions, the first appearance of visible emission (ignition) is expected to be in the shape of an umbrella. Subsequently, the flame propagates rapidly through the part of the gas mixture that is within the flammability limit in an outer envelope and resembles a flame envelope as shown in Figure 12.

Another interesting aspect is the absorption of the incident CO_2 laser beam by the fuel vapor in nitrogen atmosphere. As shown by the dashed lines

*This raises the question of the accuracy of the measurement technique upon the addition of oxidation products such as CO, CO_2 and H_2O to the assumed two molecule system. In Eq. (12), additional terms appear consisting of the mole fraction of these molecules and their refractivities. Molar refractivities for CO, CO_2 and H_2O are 5.062, 6.720 and 3.804 at 488 nm and 4.991, 6.645 and 3.748 at 633 nm, respectively (23). Wavelength dependency of these values is much closer to that of the surrounding gases used in this study than that for 1-decene. Also, concentration of these products would be small during the ignition period. Therefore, the effect of additional oxidative products on the fringe shift is expected to be small and the accuracy of the measurement is the same as discussed in Section 3.2.

in Figure 15, the temperature along the CO_2 laser beam reaches over 300°C in the center of the plume. This greatly exceeds the fuel vapor temperature near the liquid surface which is 10-30°C over the boiling temperature of 1-decene (170.5°C). Since gas phase oxidation cannot occur, the temperature rise observed in the center of the plume is due to absorption of the CO_2 laser beam, a conclusion consistent with the previous studies (28). This implies that the absorption of the CO_2 laser radiation by the fuel vapor cannot be neglected, and it appears that this heating is the key process for raising the gas phase temperature high enough to initiate the first slow global chemical reactions in the fuel vapor.

4. DEVELOPMENT OF ABSORPTION COEFFICIENT MEASUREMENT TECHNIQUE AT ELEVATED TEMPERATURES

4.1 Background

As described in the previous sections and our previous studies (28,29), it was found that one of the key mechanisms for ignition of liquid fuels by a CO_2 laser is absorption of the incident CO_2 laser beam by evolved fuel vapor in the gas phase above the irradiated surface. Since the boiling temperatures (150 ~ 200°C) of liquid fuels are much lower than the decomposition temperatures of solid fuels (300 ~ 600°C), the supplemental gas phase temperature increase caused by direct absorption of the incident laser energy for ignition of liquid fuels is critical in raising the gas phase temperature enough to initiate gas phase oxidation reactions and to reach a runaway condition. The amount of the absorption is determined by the absorption coefficient of the fuel vapor at the laser wavelength. There is extensive published absorption

data for CO, CO_2 and H_2O (30,31), but those for hydrocarbon molecules are limited to methane (31,32). Data on elevated temperature absorption spectra for large hydrocarbon molecules, which are liquids at room temperature, are extremely limited. Therefore, the measurement of the infrared absorption spectra of liquid fuel vapors at elevated temperatures is essential in order to estimate the amounts of absorbed energy and temperature increase that influence the ignitability of liquid fuel vapors.

4.2 Experimental Apparatus

A single beam infrared absorption measurement system has been constructed; a schematic illustration is given in Figure 16 and a photograph is shown in Figure 17. The system consists of a well regulated black body (~1070°C) as a radiant source, a heated cell with a water jacket (cell length is 15 cm, and a monochromator with a pyroelectric detector. The system provides low resolution spectra which might not be as accurate as using a CO_2 laser as the light source due to the narrowness of the laser line. However, the system can measure absorption spectra from 2 to 11 μm using three different snap-in type gratings. This can cover various different kinds of laser lines such as deuterium flouride, carbon dioxide, hydrogen fluoride, using the same light source. The cell can be heated to 600°C. Since ambient water vapor and carbon dioxide are good absorbers in the wavelength range of interest, the system is enclosed in an air-tight, water-cooled box, and water-pumped, dry nitrogen is purged through the box and the monochromator during the measurement. At first, the reference signal is measured by scanning the monochromator with high purity nitrogen in the heated cell at the desired elevated temperature. The signal is stored in a laboratory computer. Then,

the sample signal is measured by repeating the same scan with an appropriate concentration of a test gas brought to one atmosphere pressure by nitrogen in the cell at the same temperature as the first scan. The absorption spectrum can be calculated from the difference in the signal between the two scans. Preliminary experiments with CO_2 gas at elevated temperatures are in progress as a basis for comparison with previous studies. At present, a vapor generator for liquid fuels is under construction. Absorption spectra of decane and 1-decene at various temperatures and concentrations will be measured in the future.

5. SUMMARY

The radiative ignition mechanism of a liquid fuel by a CO_2 laser has been investigated by observing liquid behavior near the surface and measuring the distributions of temperature and fuel vapor concentration in the gas phase during the ignition period. The conclusions obtained from these experiments are as follows:

High speed photographs reveal complex behavior of the liquid surface immediately after the incident CO_2 laser irradiation. In time sequence, the formation of a radial wave, a central surface depression, bubble nucleation/growth/bursting, followed by complex surface motion and further bubbling, were observed; typically several (or many) bubble cycles precede ignition. It appears that volumetric liquid expansion and photon pressure cause the initial radial wave movement, and the subsequent surface depression is caused by the reaction force of plume-like vaporization. Soon the sub-surface layer of the liquid has achieved appreciable superheating which results in bubble nucleation probably on heterogeneous nuclei.

There are clear trends of behavior with increasing incident laser flux or fuel absorptivity; increases in either accelerate the whole sequence of events, lead to a dominance of bubbling phenomena and decrease the ignition delay. An order of magnitude analysis indicates that the motion in the liquid caused by temperature gradients does not have significant affects on the vaporization process at least in the high end of the flux range in this study.

There are three idealized limiting cases of vaporization behavior that facilitate analysis of the gas phase vapor build-up and subsequent ignition. The first is the purely stable, non-turbulent vaporization case in which a bubble never occurs. The second limiting case is that of very low frequency bubbling superposed on the stable plume vaporization, which appears at medium laser fluxes. The third limiting case corresponds to high frequency, large bubble bursts. To the gas phase this presents a roughly constant, non-directional vapor source. These limiting cases are more amenable to at least approximate theoretical analysis.

An increase in oxygen concentration in the environmental gas phase decreases the distance between the liquid surface and the location of the first appearance of visible emission which is defined as ignition in this study. However, the distance is independent of an increase in peak laser flux within the range used in this study. Oxygen in the gas phase significantly increases the growth rate of the plume shortly after the appearance of fuel vapor at the same peak laser fluxes.

Prior to ignition, there are two global chemical reaction stages in the gas phase, similar to those for a solid fuel: one is a relatively slow

process starting at an early stage after the appearance of the plume with temperatures up to about 400-450°C; the other is a significantly faster process occurring just before ignition at temperatures above 450-500°C.

A significant temperature increase (more than 100°C) was found in the center of the plume in a nitrogen atmosphere, and is attributed to the absorption of the incident CO_2 laser beam by fuel vapor.

6. ACKNOWLEDGMENT

The authors would like to thank Mr. William H. Wooden for his assistance in conducting experiments.

7. REFERENCES

1. Kashiwagi, T. "Ignition of a Liquid Fuel Under High Intensity Radiation," Comb. Sci. Tech. 21, p. 131 (1980).

2. Kashiwagi, T., Baum, H. R., and Rockett, J. A. "Ignition of a Liquid Fuel Under High Intensity Radiation," AFOSR-TR-80-0476 (1980).

3. Bergman, T. and Mesler, R. "Bubble Nucleation Studies, Part 1: Formation of Bubble Nuclei in Superheated Water by Bursting Bubbles," AIChE J., 27, p. 851 (1981).

4. Carroll, K. and Mesler, R. "Bubble Nucleation Studies, Part 2: Bubble Entrainment by Drop-Formed Vortex Ring," 27, p. 853 (1981).

5. Texas A and M University, Selected Infrared Spectral Data, American Petroleum Institute Research Project 44, Vol. 3 (1977).

6. Handbook of Chemistry and Physics, Edited by R. C. Weast, The Chemical Rubber Co. Press (1969).

7. Handbook of Tables for Applied Engineering Science, The Chemical Rubber Co. Press, p. 388 (1973).

8. Cole, R. "Boiling Nucleation" in Advances in Heat Transfer (J. P. Hartnett and T. F. Irvine, Eds.), Academic Press, Vol. 10 (1974).

9. Blander, M. and Katz, J. L. "Bubble Nucleation in Liquids," AIChE J., 21, p. 833 (1975).

10. Reid, R. C. "Superheated Liquids," American Scientist, Vol. 64, p. 146 (1976).

11. Porteous, W. and Blander, M. "Limits of Superheat and Explosive Boiling of Light Hydrocarbons, Halocarbons, and Hydrocarbon Mixtures," AIChE J., Vol. 21, p. 560 (1975).

12. Ward, C. A., Balakrishnan, A., and Hooper, F. C. "On the Thermodynamics of Nucleation in Weak Gas-Liquid Solutions," J. Basic Eng., D92, p. 695 (1970).

13. Mori, Y., Hijikata, K., and Nagatani, T. "Effects of Dissolved Gas on Bubble Nucleation," Int. J. Heat Mass Transfer, 19, p. 1153 (1976).

14. Lauterborn, W. and Bolle, H. "Experimental Investigations of Cavitation-Bubble Collapse in the Neighborhood of a Solid Boundary," J. Fluid Mech., 72, p. 391 (1975).

15. Hsu, Y. Y. and Graham, R. W. Transport Processes in Boiling and Two-Phase Systems, McGraw-Hill Book Co., (1976).

16. Murad, R. J., Larendola, J., Isoda, H., and Summerfield, H. "A Study of Some Factors Influencing the Ignition of a Liquid Fuel Pool," Comb. Flame, 15, p. 289 (1970).

17. Ohlemiller, T. J. and Summerfield, M. "Radiative Ignition of Polymeric Materials in Oxygen/Nitrogen Mixture," Thirteenth Symposium (International) on Combustion, The Combustion Institute, p. 1087 (1971).

18. Mutoh, N., Hirano, T., and Akita, K. "Experimental Study of Radiative Ignition of Polymethylmethacrylate," Seventeenth Symposium (International) on Combustion, The Combustion Institute, p. 1183 (1978).

19. El-Wakil, M. M. and Ross, P. A. "A Two-Wavelength Interferometric Technique for the Study of Vaporization and Combustion on Fuels," Liquid Rockets and Propellants, Progress in Astronautics and Rocketry, Vol. 2, Academic Press, New York (1960).

20. Mayinger, F. and Panknin, W. "Holography in Heat and Mass Transfer," Proceeding of Fifth International Heat Transfer Conference, Vol. 6, p. 28 (1974).

21. Mayinger, F. and Panknin, W. "Holographic Two-Wavelengths Interferometry for Measurement of Combined Heat and Mass Transfer," Combustion Measurements (R. Goulard, Ed.), Academic Press, New York, p. 270 (1976).

22. Vest, C. M. Holographic Interferometry, John Wiley and Sons, New York, Chapter 6 (1979).

23. Gardiner, W. C., Hidaka, Y., and Tanzawa, T. "Refractivity of Combustion Gases," Combust. Flame, 40, p. 213 (1981).

24. Kashiwagi, T. and Kashiwagi, T. "A Study of the Radiative Ignition Mechanism of a Solid Fuel Using Holographic Interferometry," AIAA-82-0238, AIAA 20th Aerospace Sciences Meeting, Orlando, Florida, January 1982.

25. Ohlemiller, T. J. and Summerfield, M. "Radiative Ignition of Polymeric Materials in Oxygen/Nitrogen Mixtures," Thirteenth Symposium (International) on Combustion, The Combustion Institute, p. 1087 (1971).

26. Gray, P., Griffiths, J. F., Hasko, S. M., and Lignola, P. G. Proc. Roy. Soc. London A374, p. 313 (1981).

27. Zabetakis, M. G. "Flammability Characteristics of Combustible Gases and Vapors," Bulletin 627, Bureau of Mines, 1965.

28. Kashiwagi, T. Combust. Flame 34, p. 231 (1979).

29. Kashiwagi, T. "Radiative Ignition Mechanism of Solid Fuels," Fire Safety J. 3, p. 185 (1981).

30. Hottel, H. C. and Sarofim, A. F. Radiative Transfer, McGraw-Hill Book Co., Chapter 6, 1967.

31. Edwards, D. K. and Balakrishnan, A. "Thermal Radiation by Combustion Gases," Int. J. Heat Mass Transfer, 16, p. 25 (1973).

32. Lee, R. H. C. and Happel, J. "Thermal Radiation of Methane Gas," I/EC Fundamentals 3, p. 167 (1964).

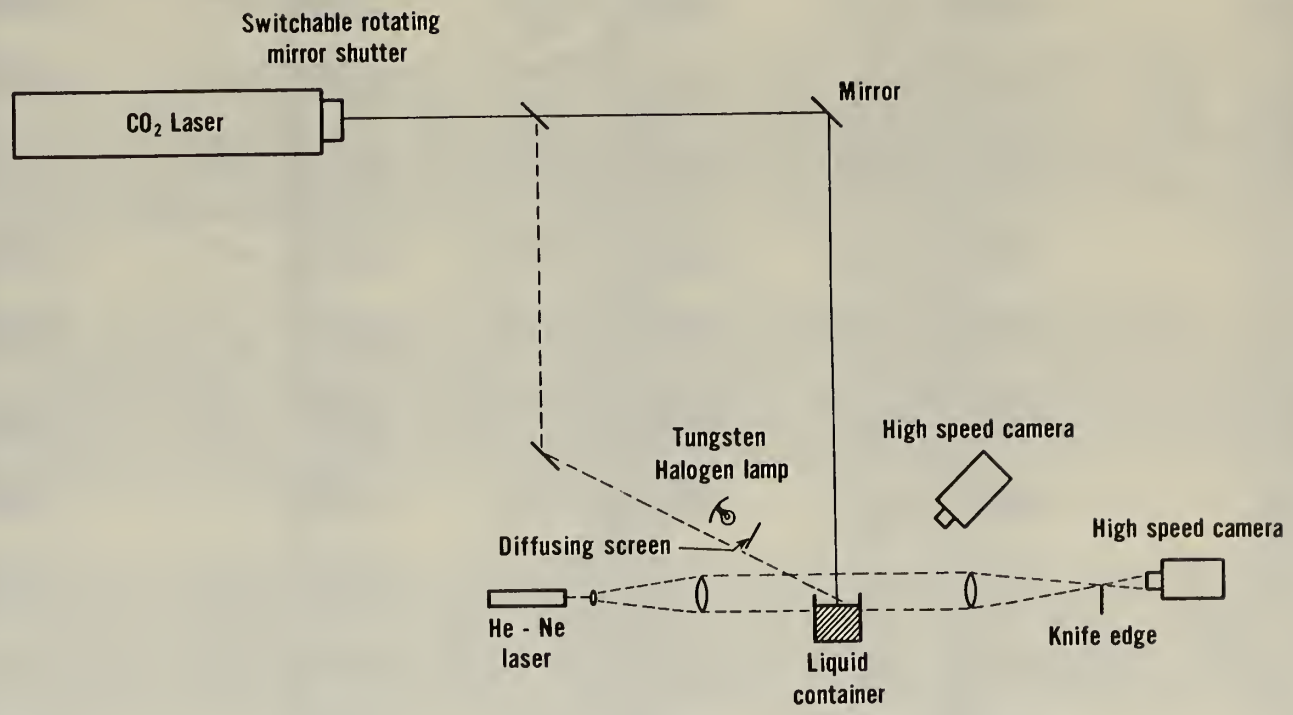

Fig. 1. Schematic illustration of experimental apparatus for observation of liquid behavior and vapor generation

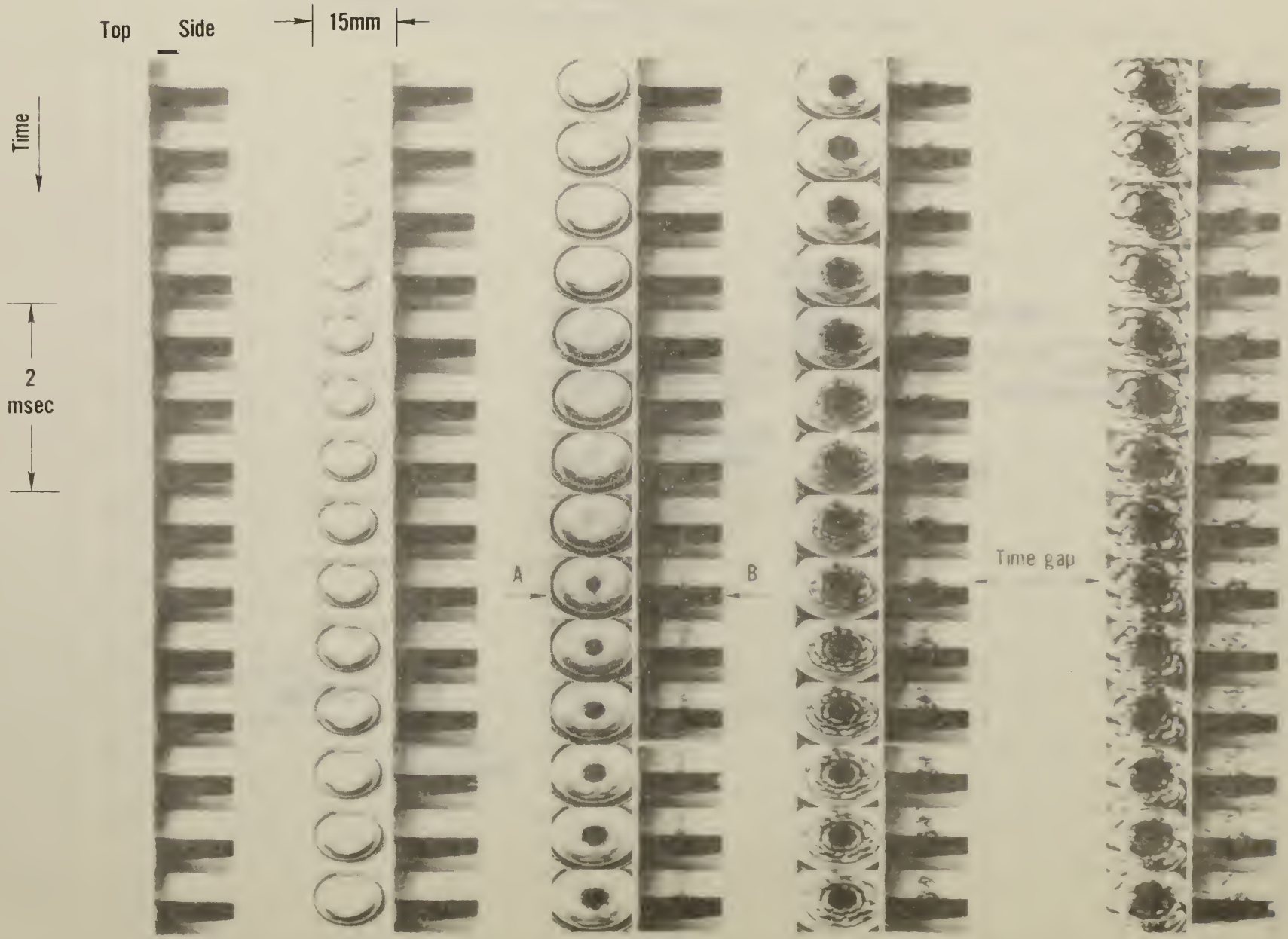

Fig. 2. Top view direct picture and side view schlieren picture; left columns, top view; right columns, side view. Decane, laser flux of 740 W/cm^2, incident laser angle of 30 degrees. A, appearance of hole due to first bubble in top view; B, corresponding sudden release of liquid vapor. Time gap about 30 msec

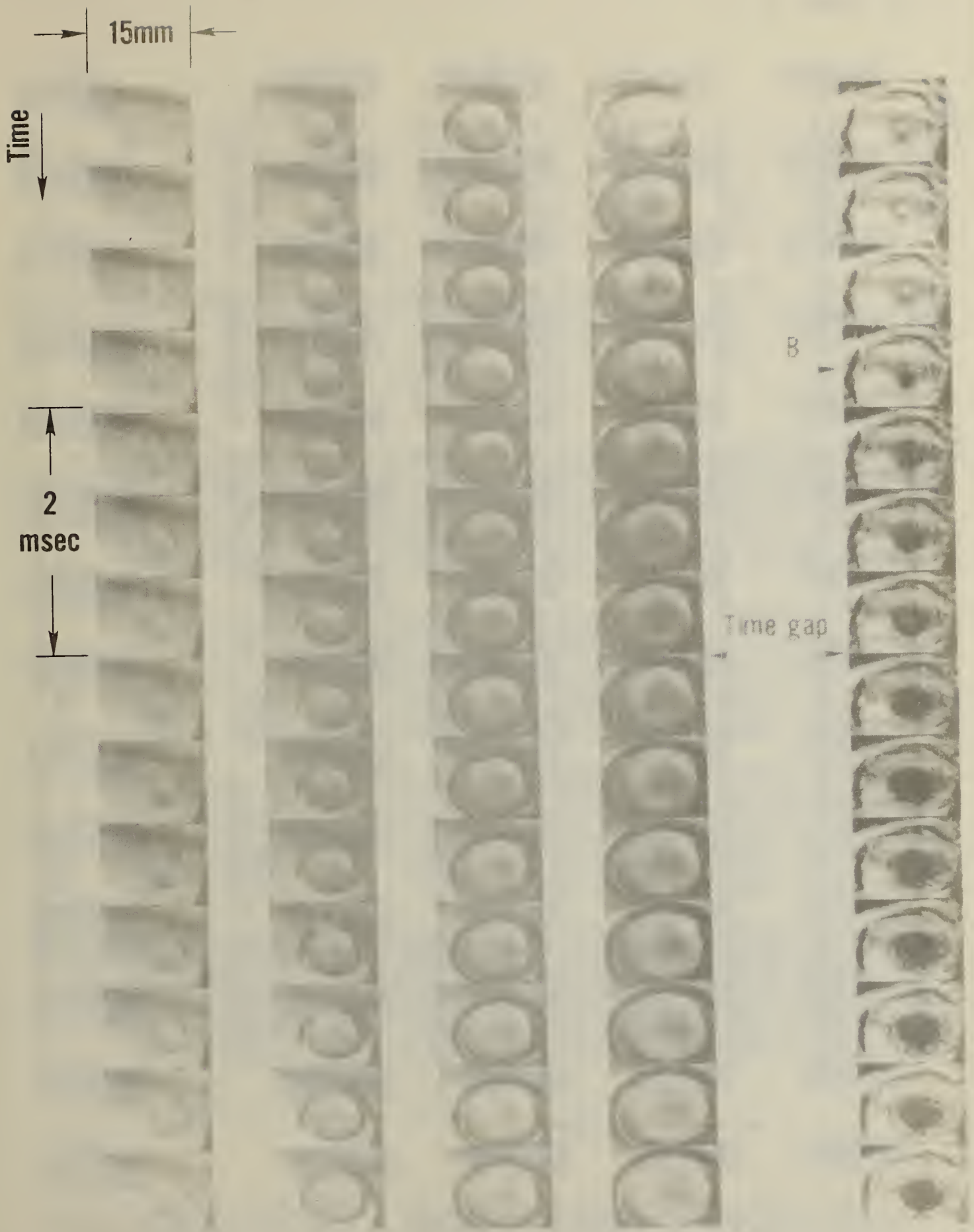

Fig. 3a. Top view picture, decane, laser flux of 410 W/cm^2 and incident laser angle of 30 degrees; B, appearance of hole due to first bubble. Time gap, about 350 msec

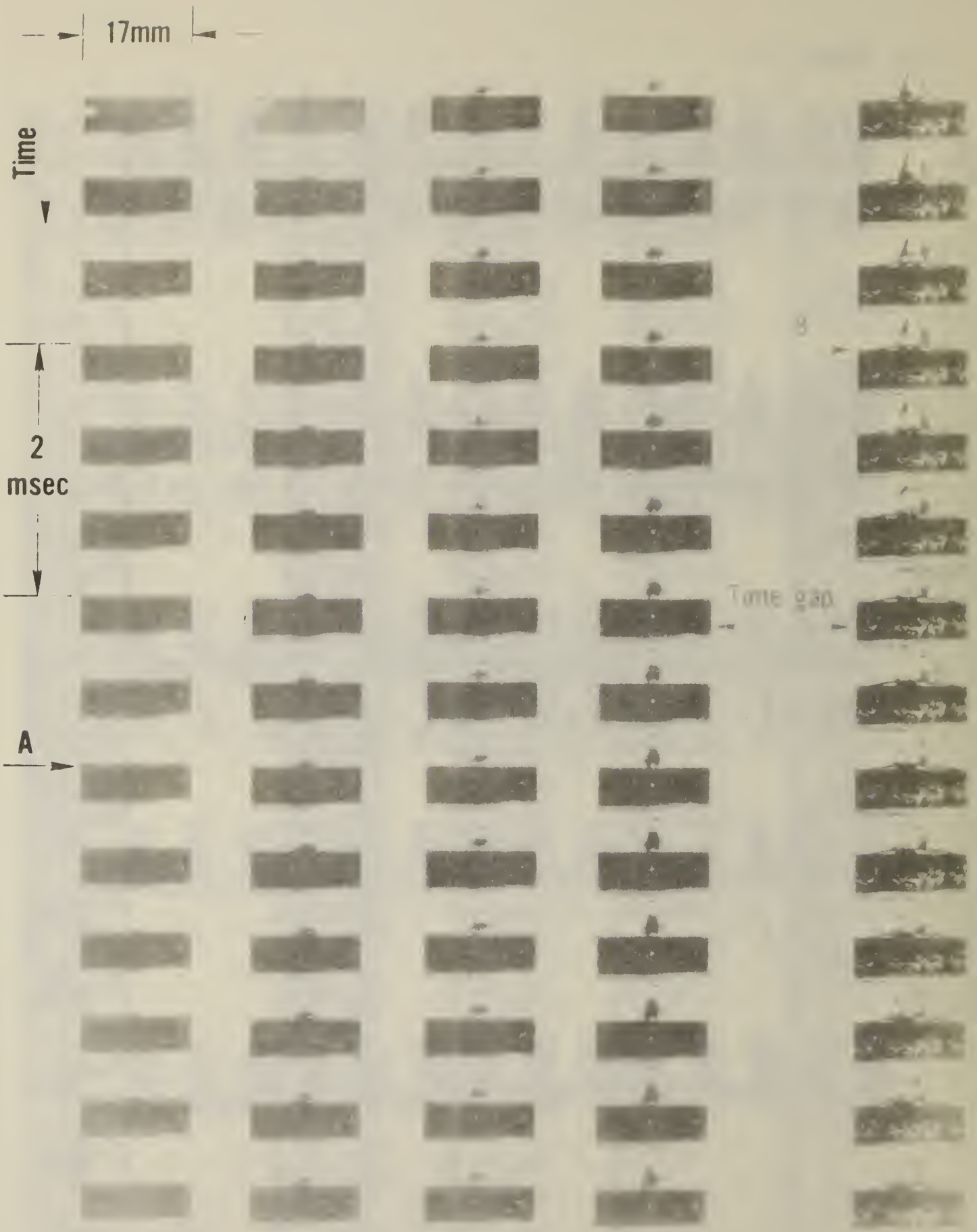

Fig. 3b. Side view schlieren picture, same test as Figure 3a. A, appearance of laminar vapor plume; B, sudden release of liquid vapor by bubble burst

Fig. 4. Side view closeup direct picture near the decane surface, laser flux of about 2500 W/cm^2 with incident laser angle of 30 degrees from right to left

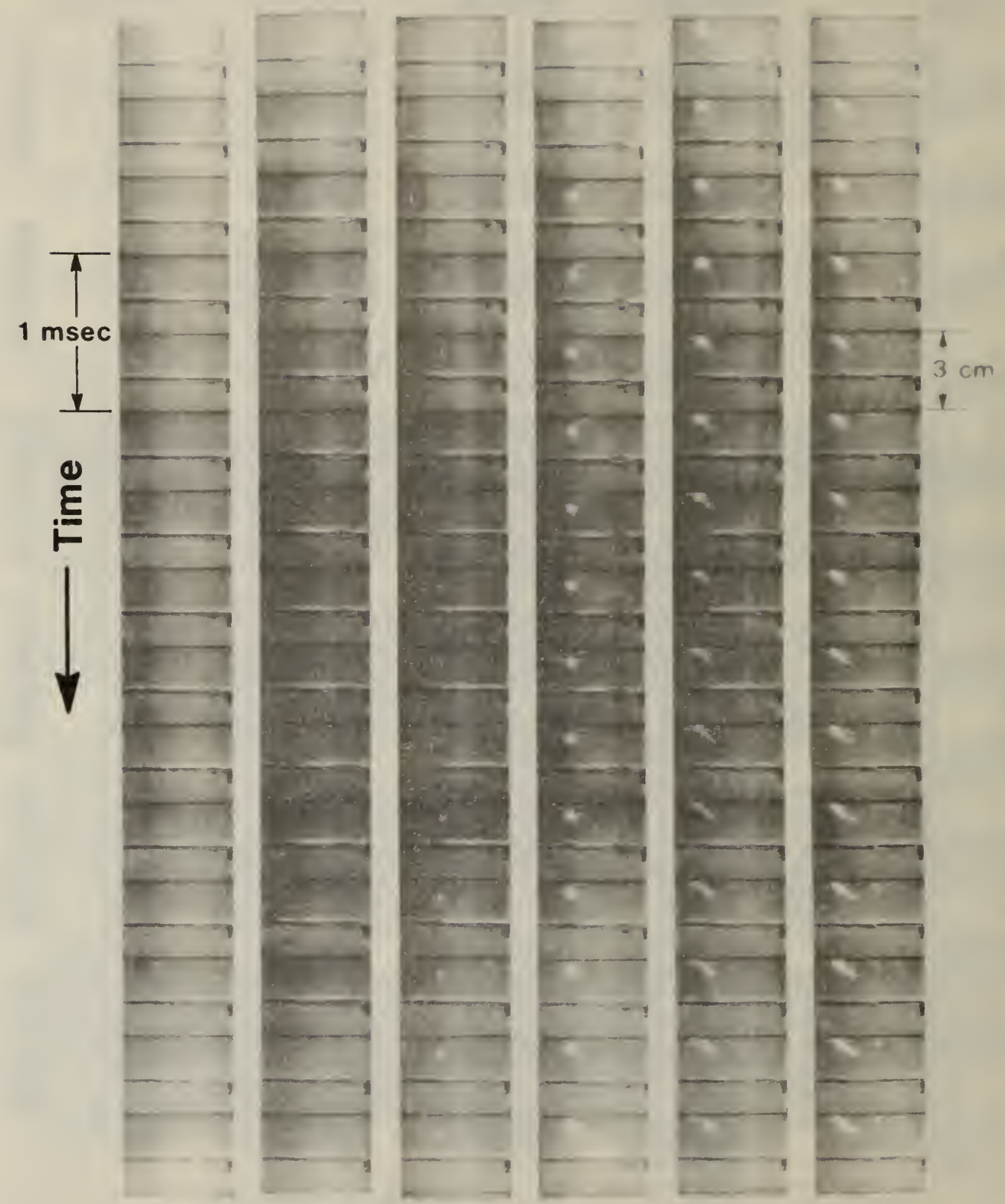

Fig. 5. Side view direct picture to show the location of the first appearance of flame. Decane at a laser flux of about 2500 W/cm^2 with incident laser angle of 30 degrees from left to right

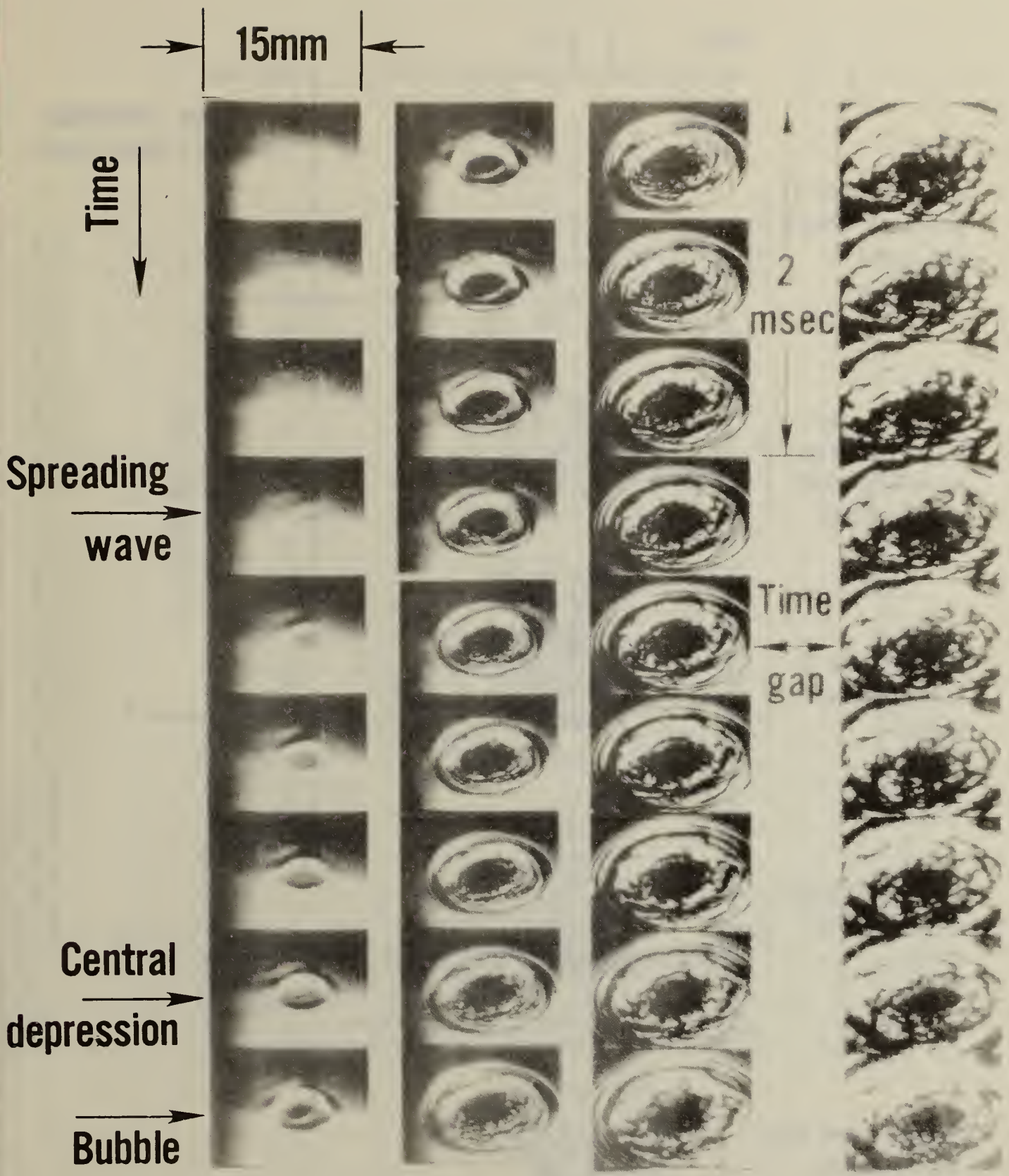

Fig. 6. Top view picture of decene with laser flux of 910 W/cm^2 and incident laser angle of 90 degrees. Time gap is about 18 msec

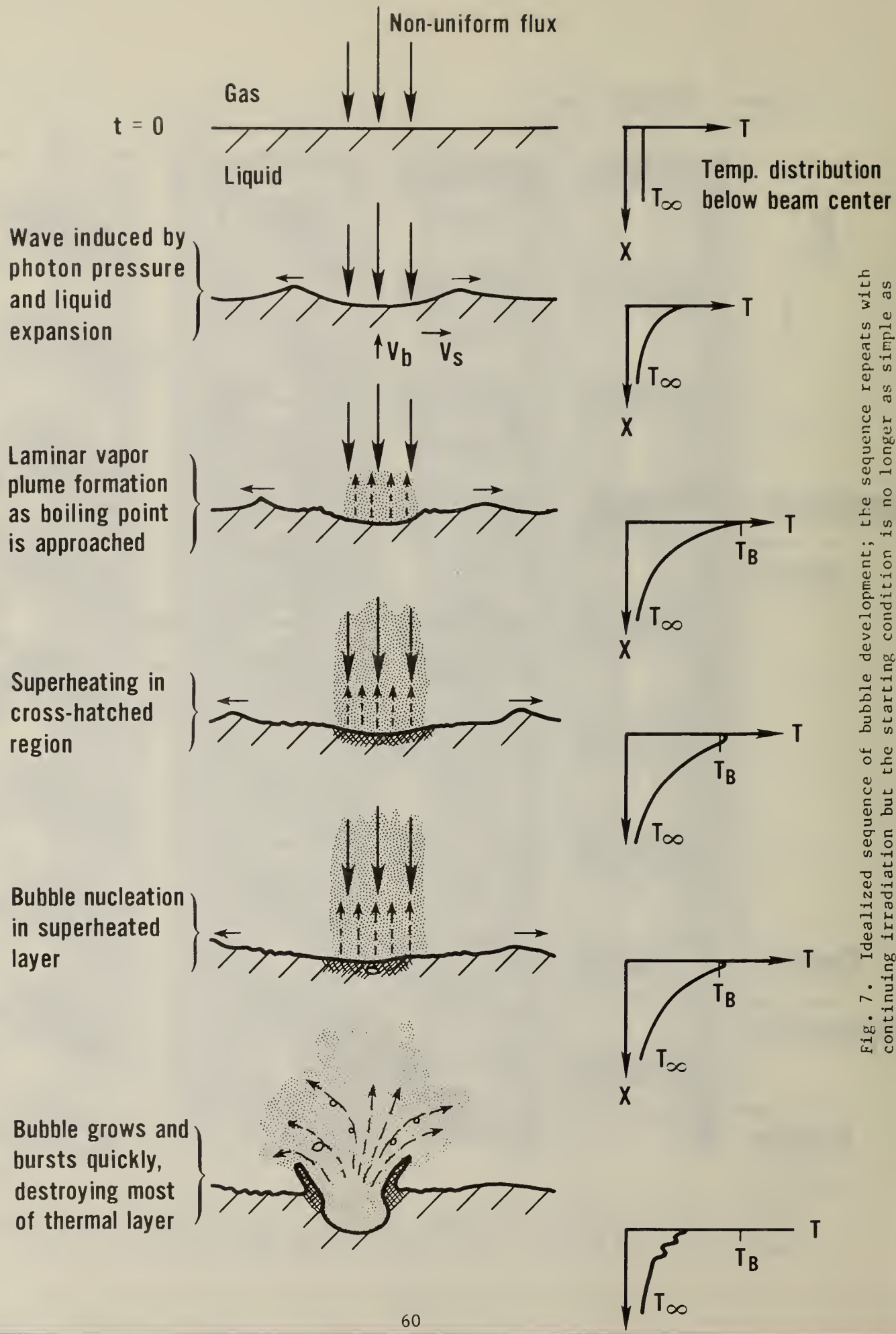

Fig. 7. Idealized sequence of bubble development; the sequence repeats with continuing irradiation but the starting condition is no longer as simple as that in the first sketch

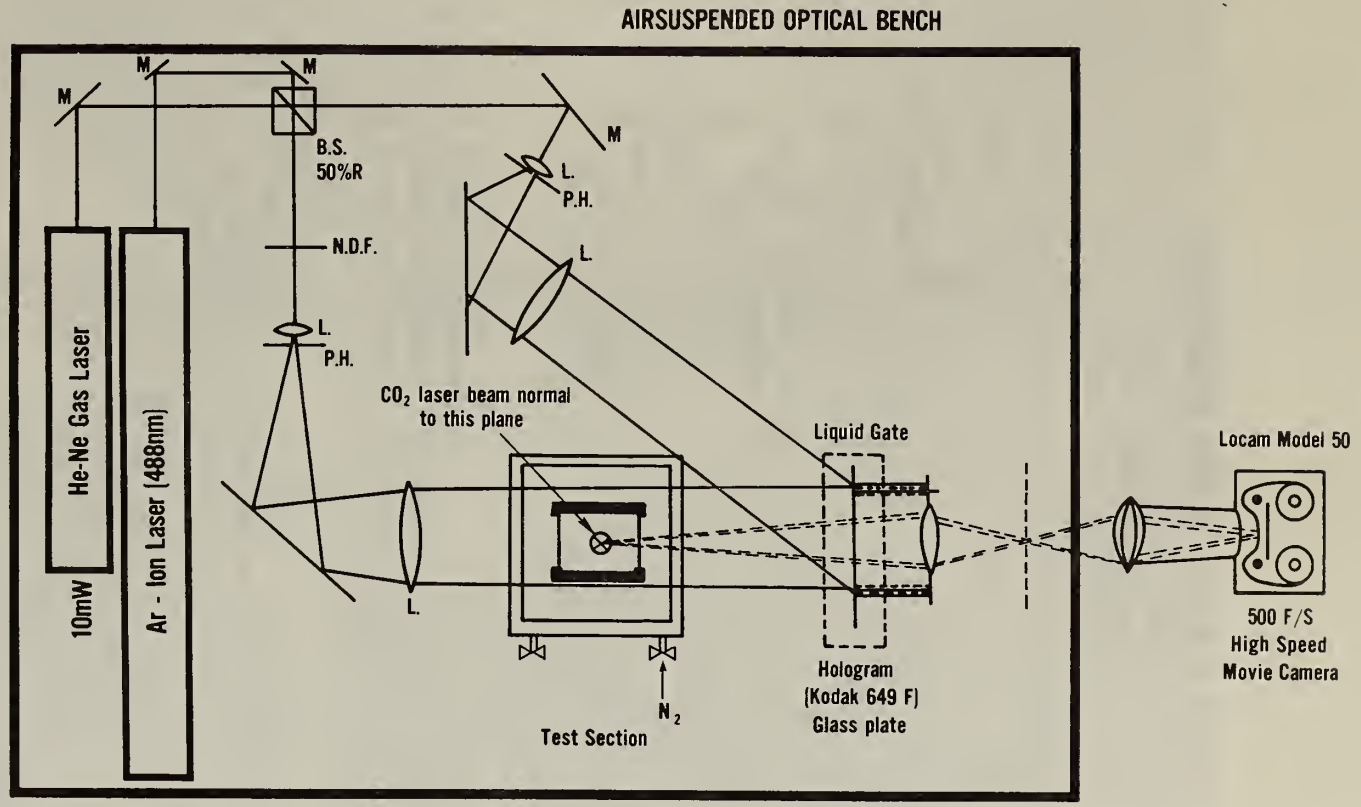

Fig. 8. Schematic illustration of experimental set-up of high speed two-wavelength holographic interferometer

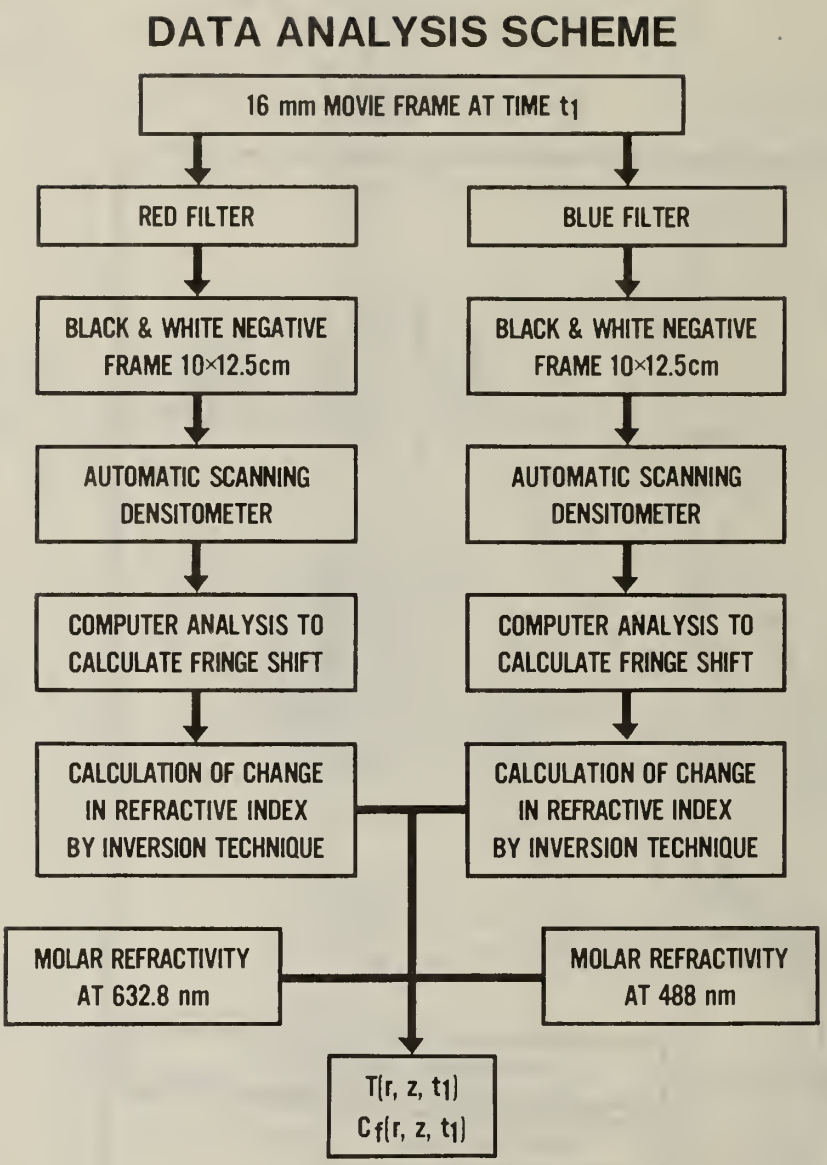

Fig. 9. Data analysis scheme from 16 mm movie frames

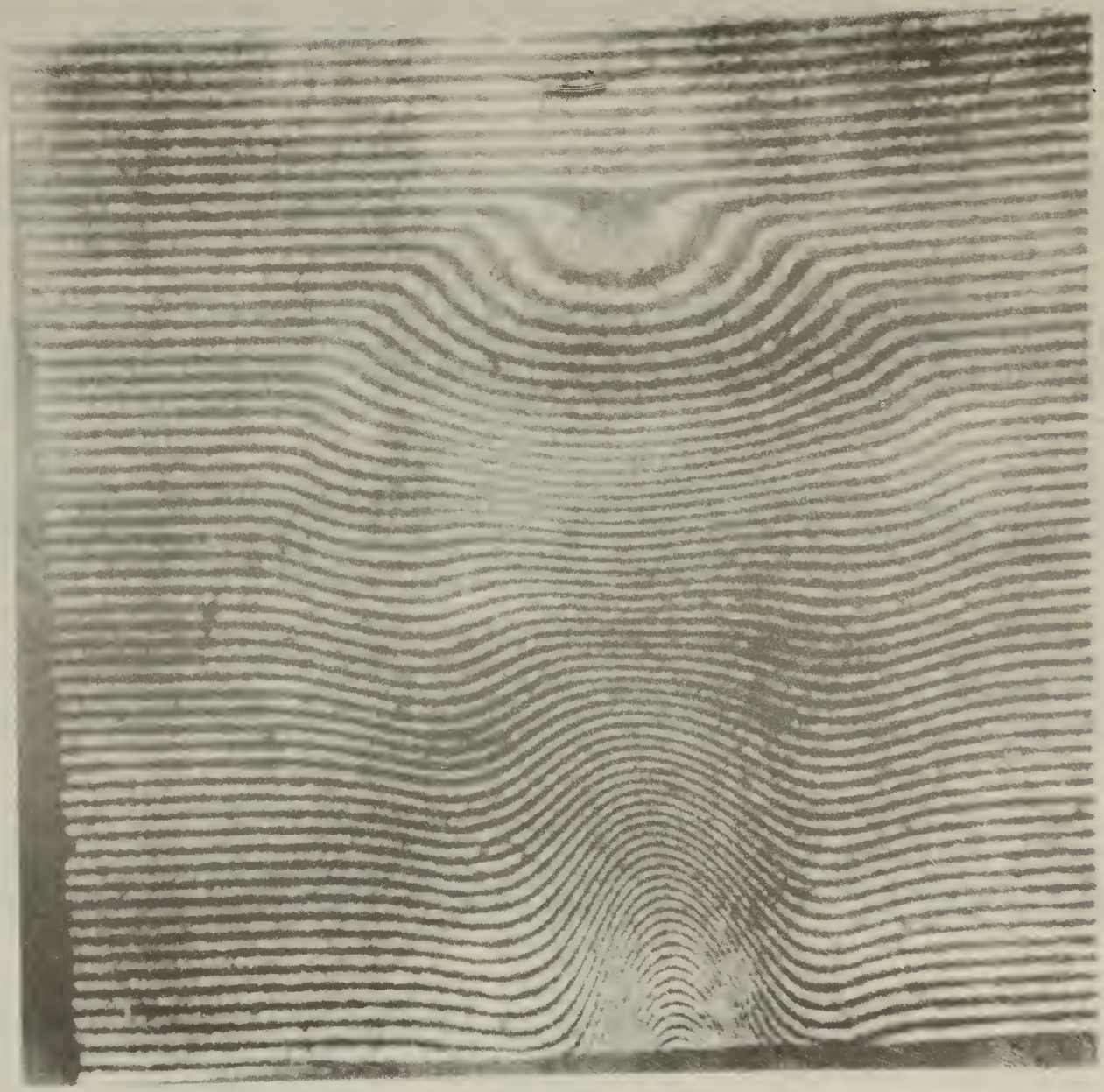

Fig. 10. Interferogram reconstructed by computer for blue light with 1-decene

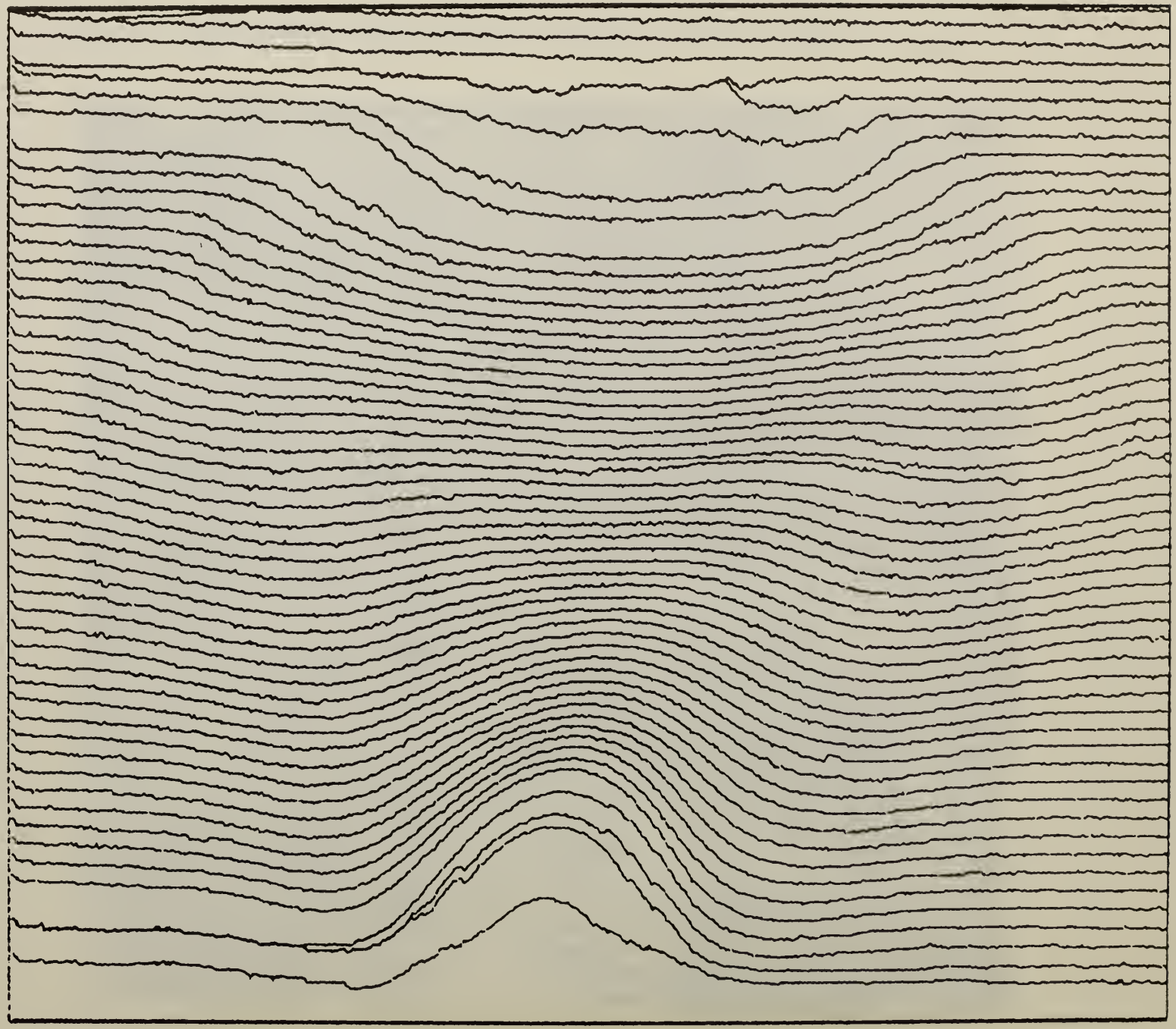

Fig. 11. Computer calculated contour plot of peaks of fringes, 1-decene and blue light

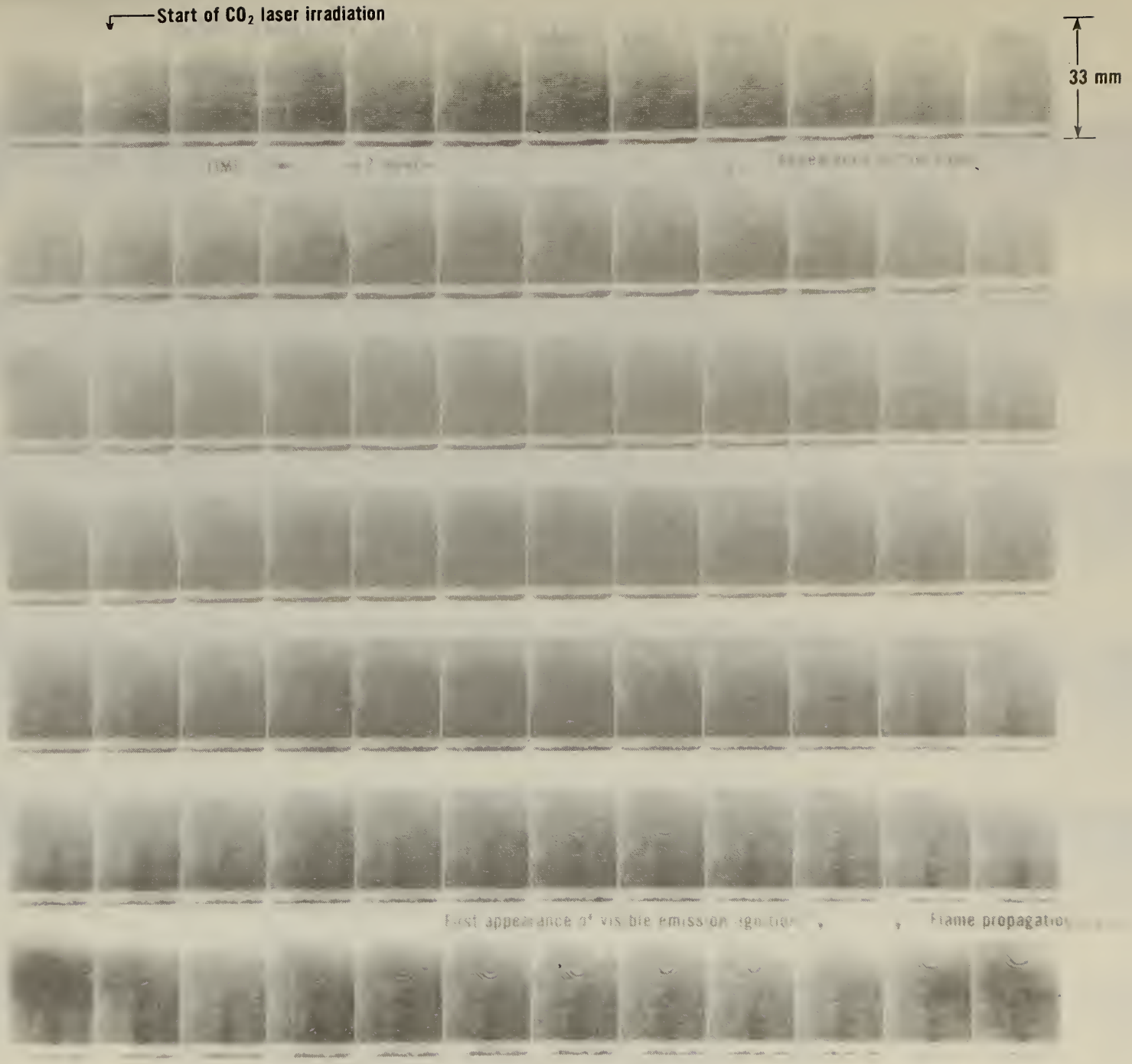

Fig. 12a. Typical results of the interferogram motion pictures made at 500 frames per second at wavelength 632.8 nm, peak laser flux at 260 W/cm^2 with air

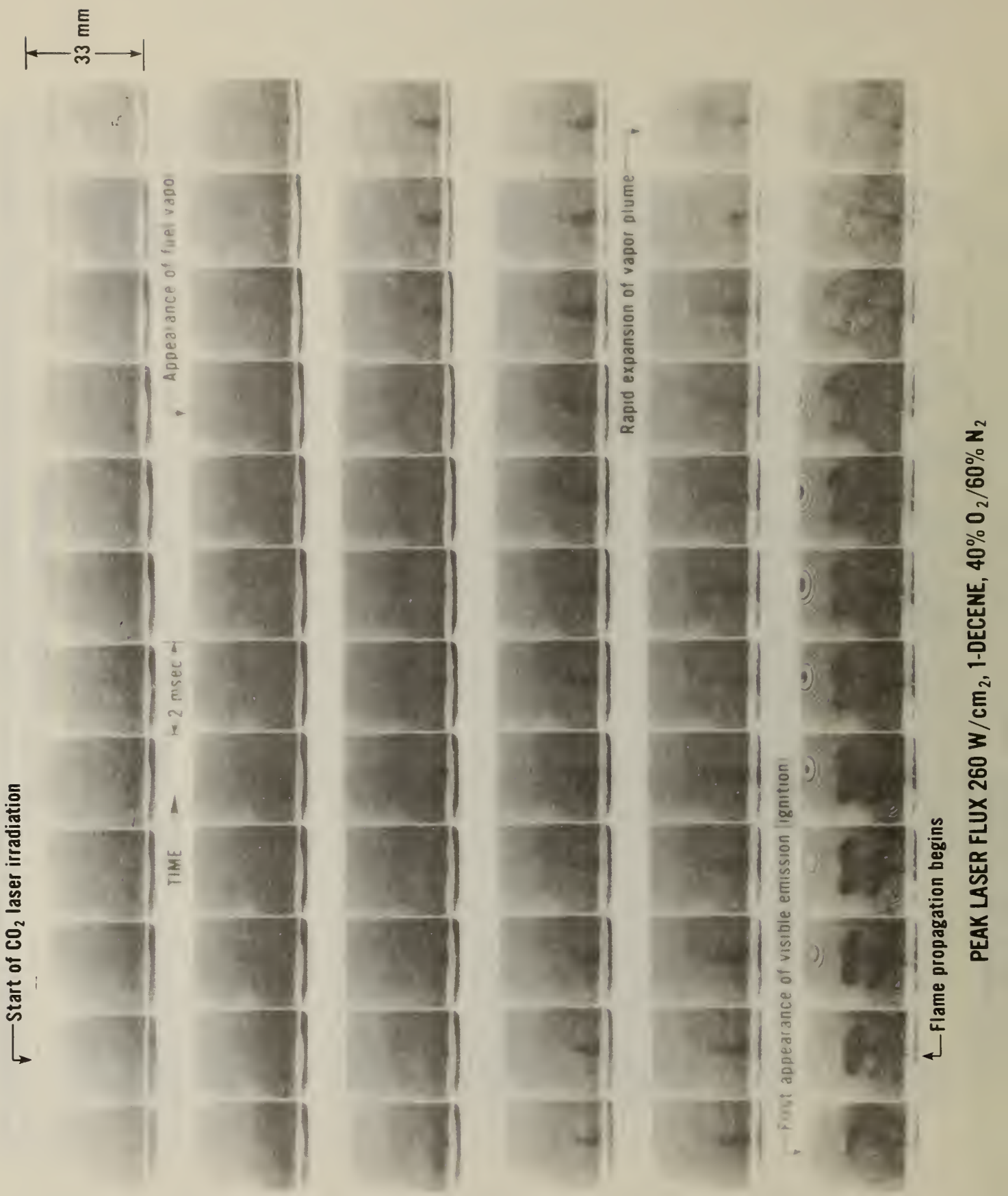

Fig. 12b. Typical results of the interferogram motion pictures made at 500 frames per second at wavelength 632.8 nm, peak laser flux at 260 W/cm^2 with 40% O_2/60% N_2.

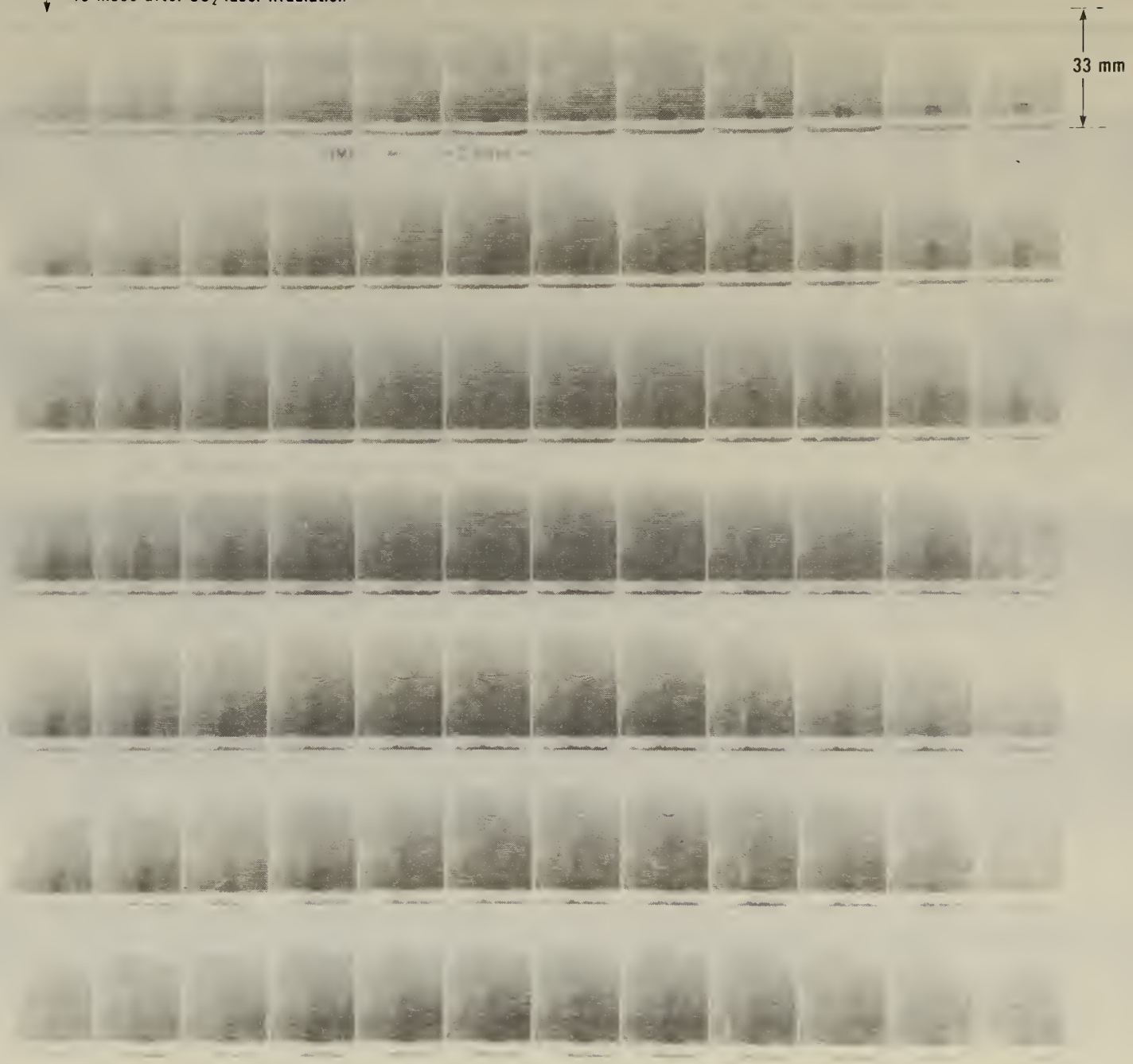

Fig. 12c. Typical results of the interferogram motion pictures made at 500 frames per second at wavelength 632.8 nm, peak laser flux at 260 W/cm^2 with N_2.

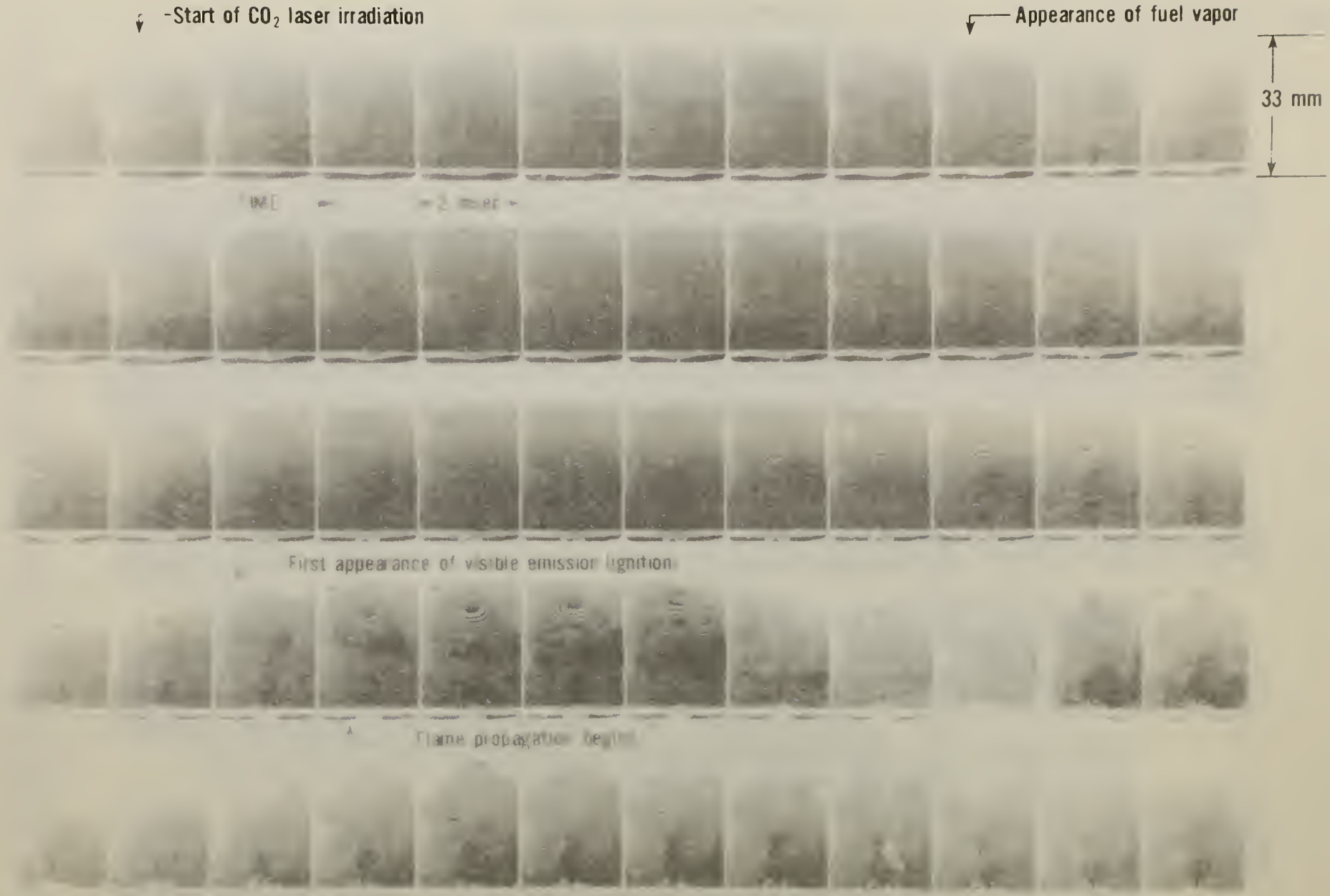

Fig. 13. Interferogram motion pictures made at 500 frames per second at wavelength 632.8 nm, peak laser flux at 520 W/cm^2 with air environment

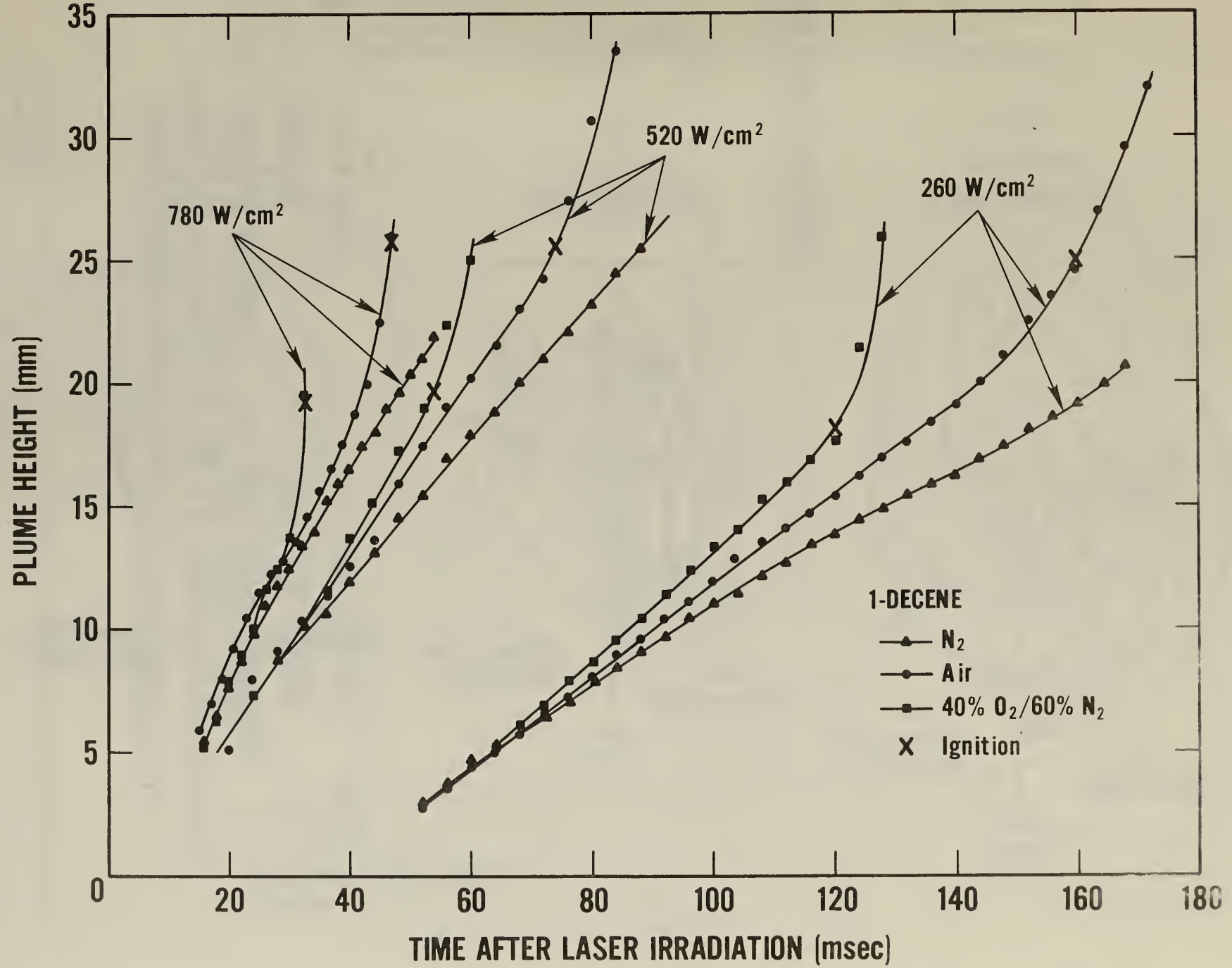

Fig. 14. Comparison in the growth of the fuel vapor plume height with three different environmental gases at three different peak laser fluxes

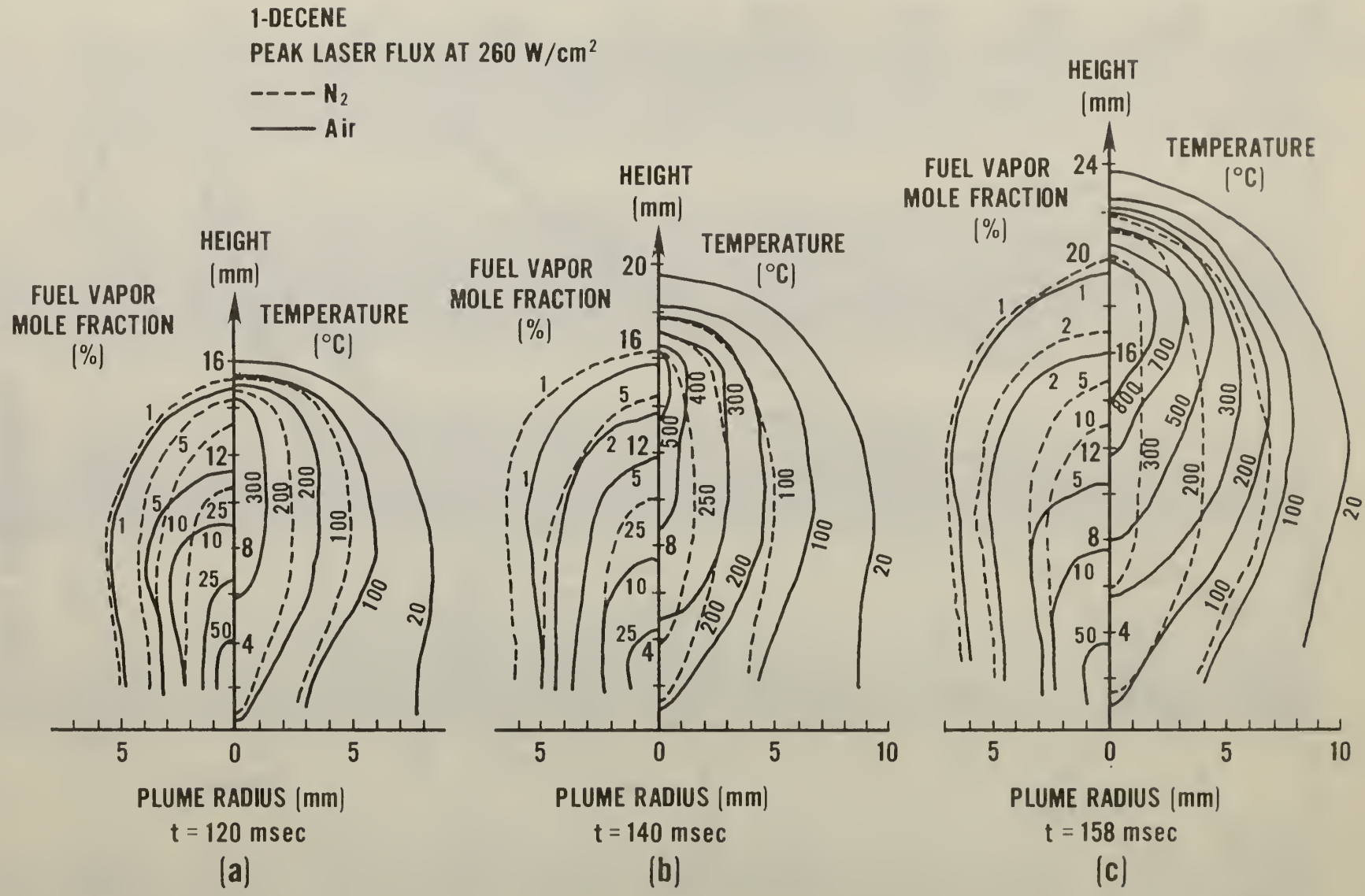

Fig. 15. Comparison of temperature and fuel vapor concentration distributions between air and nitrogen environments at (a) 120 msec, (b) 140 msec, (c) 158 msec from the start of the CO_2 laser irradiation, ignition delay time 160 msec, peak laser flux at 260 W/cm^2.

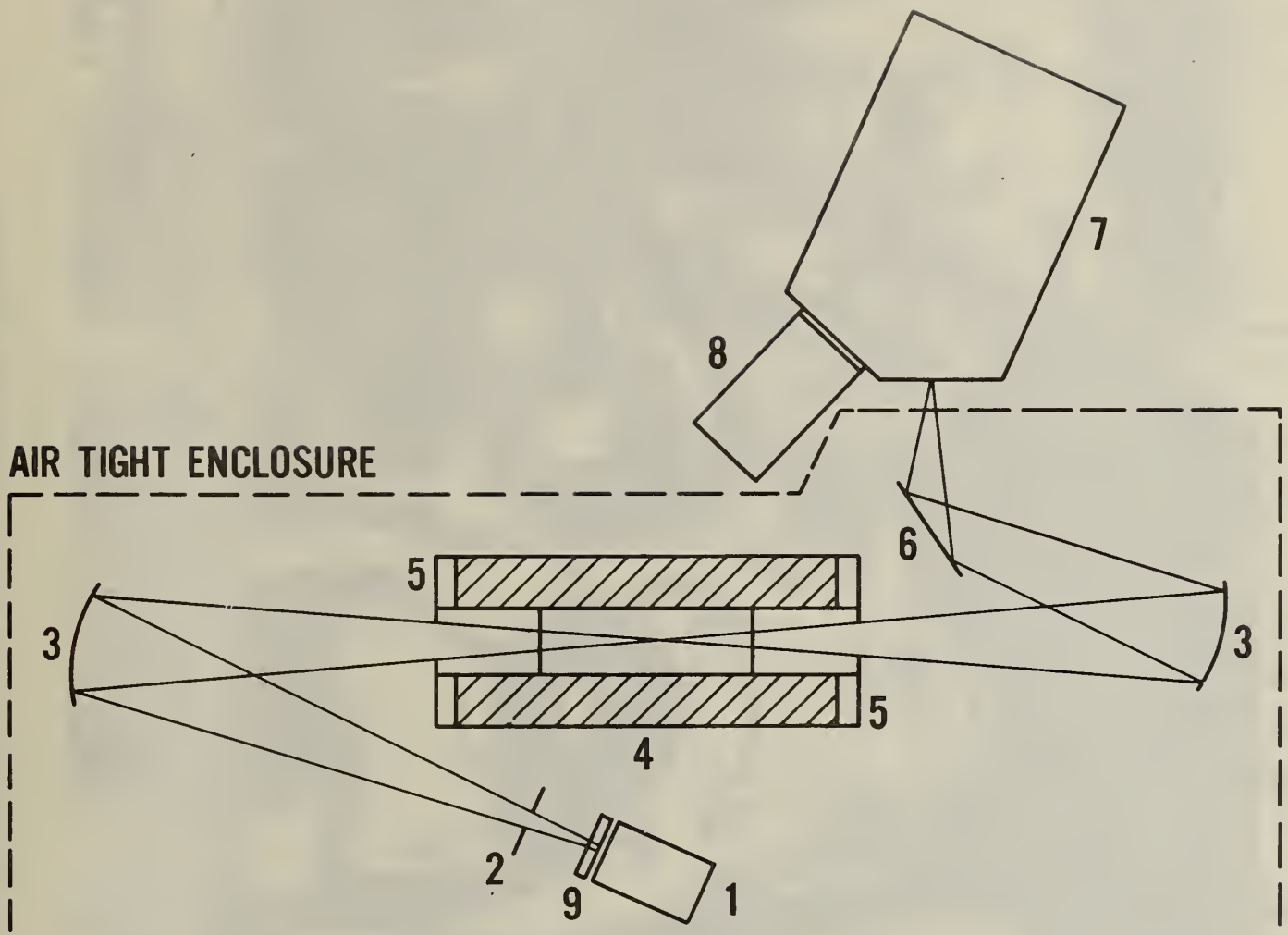

1. BLACK BODY
2. CHOPPER
3. CONCAVE MIRRORS
4. HEATED CELL WITH WATER COOLED JACKET
5. WATER COOLED SHIELDS
6. FLAT MIRROR
7. MONOCHROMATOR
8. PYROELECTRIC DETECTOR
9. WATER COOLED SLIT

Fig. 16. Schematic illustration of infrared absorption spectra measurement apparatus

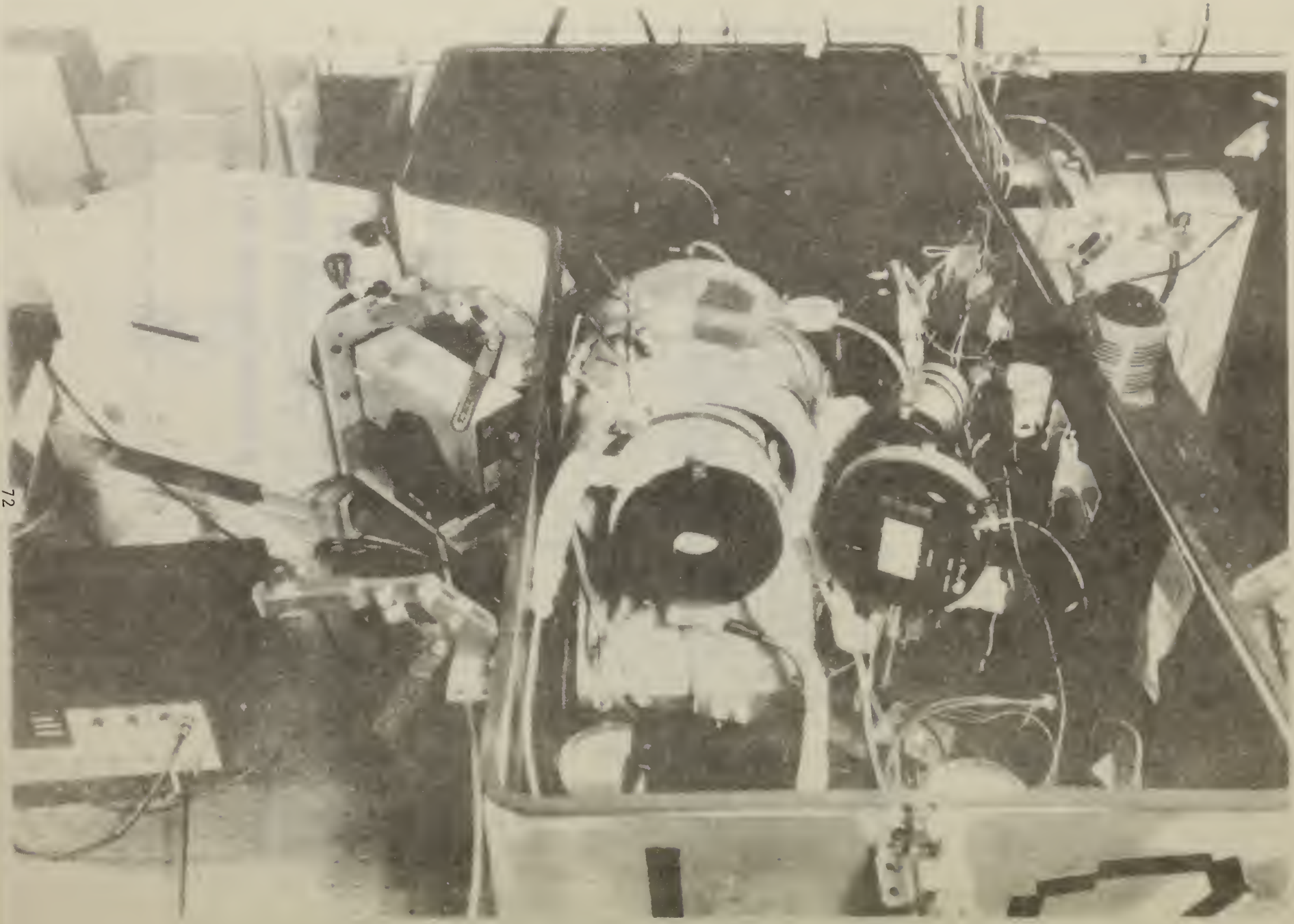

Fig. 17. Picture of infrared absorption spectra measurement apparatus

DISTRIBUTION LIST

AFWAL/POSH (10 cys)
WPAFB, OH 45433

AFWAL/FIBC
ATTN: F. E. Barnett
WPAFB, OH 45433

AFWAL/FIES
ATTN: R. W. Lauzze
WPAFB, OH 45433

AFWAL/FIES/CDIC
WPAFB, OH 45433

AFWAL/FIMG
ATTN: A. B. Lewis
WPAFB, OH 45433

AFWAL/MLPJ
ATTN: G. L. Denman
WPAFB, OH 45433

AFWAL/TST (Library)
WPAFB, OH 45433

AFWAL/TST-PO (STINFO)
WPAFB, OH 45433

ASD/XRJ
ATTN: L. R. Roesner
WPAFB, OH 45433

ASD/XROT
ATTN: G. Bennett
WPAFB, OH 45433

FTD/SDNS
ATTN: Everett Henderson
WPAFB, OH 45433

FTD/TQTD
ATTN: V. J. Slaboszewicz
WPAFB, OH 45433

AFWL/ARAC
ATTN: Paul J. Ortwerth
Kirtland AFB, NM 87117

AFWL/AREE
ATTN: Lt. Col. D. A. Carey
Kirtland AFB, NM 87117

AFWL/AREE
ATTN: Allen F. Gunther
Kirtland AFB, NM 87117

AFWL/AREE
ATTN: W. T. Laughlin
Kirtland AFB, NM 87117

AFWL/AREE
ATTN: Freidrich Peyerl
Kirtland AFB, NM 87117

AFWL/AREE
ATTN: Ralph R. Rudder
Kirtland AFB, NM 87117

AFWL/AREP
ATTN: Robert F. Walter
Kirtland AFB, NM 87117

AFWL/ARLO
ATTN: Lt. Col. L. Jungling
Kirtland AFB, NM 87117

HQ AFSC/DLFP
ATTN: Mr. Wm. Supp
Andrews AFB, DC 20334

HQ AFSC/DLWM
ATTN: Maj. J. O'Prey
Andrews AFB, DC 20334

Office of the Secretary of Defense
ATTN: J. R. Airey
The Pentagon, Rm. 3D1067
Washington, D.C. 20301

Defense Intelligence Agency
ATTN: Seymour Berler
The Pentagon, DT-1A
Washington, D.C. 20301

Naval Postgraduate School
ATTN: R. E. Ball (678P)
Monterey, CA 93940

U.S. Army Ballistic Research
Laboratory
ATTN: D. W. Mowrer (DRDAR/BLV)
Aberdeen Proving Ground, MD 21005

U.S. Army Ballistic Research Laboratory
ATTN: Richard D. Miller (DRDAR/BLV)
Aberdeen Proving Ground, MD 21005

U.S. Army Ballistic Research Laboratory
ATTN: John H. McNeilly (DRDAR/BLV)
Aberdeen Proving Ground, MD 21005

Applied Technology Laboratory
U.S. Army Rsch. & Tech. Labs.
ATTN: C. Pedriani (DAVDL-ATL-ASV)
Fort Eustis, VA 23604

Applied Technology Laboratory
U.S. Army Rsch. & Tech. Labs.
ATTN: E. Gilbert (DAVDL-EV-MOS)
Fort Eustis, VA 23604

U.S. Army Missile Rsch. & Dev. Command
ATTN: Raymond W. Conrad (DRSMI-RHC)
Redstone Arsenal, AL 35809

U.S. Army Missile Rsch. & Dev. Command
ATTN: Ronald W. Mitchell
(DRCPM-HEL-T)
Redstone Arsenal, AL 35809

Naval Weapons Center
ATTN: K. W. Bailey, Code 3183
China Lake, CA 93555

Naval Weapons Center
ATTN: Conrad Driussi, Code 4011
China Lake, CA 93555

Defense Technical Information Center
ATTN: DDA
Cameron Station
Alexandria, VA 22314

Naval Sea Systems Command
ATTN: Alfred L. Stoessell
PMS 405-30
Washington, D.C. 20362

Boeing Aerospace Company
ATTN: Richard B. Hall
PO Box 3999, MS 88-46
Seattle, WA 98124

Boeing Military Airplane Company
ATTN: V. K. Rajpaul
PO Box 3707
Seattle, WA 98124

Falcon Rsch. & Dev. Company
ATTN: L. Mahood
109 Inverness Drive East
Englewood, CA 80112

McDonnell Aircraft Company
ATTN: E. Wiggins
Dept. 353, Bldg. 33-6-660
PO Box 516, Lambert Field
St Louis, MO 63166

McDonnell Aircraft Company
ATTN: E. R. Lake
Dept. 353, Bldg. 32
PO Box 516
St Louis, MO 63166

Atlantic Research Corporation
ATTN: M. K. King
5390 Cherokee Avenue
Alexandria, VA 22314

AVCO Corporation
AVCO Everett Research Laboratory Division
ATTN: D. Stickler
2385 Revere Beach Parkway
Everett, MA 02149

Science Applications, Inc.
ATTN: R. B. Edelman
Combustion Dynamics and Propulsion Division
23146 Cumorah Crest
Woodland Hills, CA 91364

Battelle Memorial Institute
ATTN: Technical Library
R. Bartlett
505 King Avenue
Columbus, OH 43201

Case Western Reserve University
Division of Aerospace Sciences
ATTN: J. Tien
Cleveland, OH 44135

Georgia Institute of Technology
School of Aerospace Engineering
ATTN: B. T. Zinn
E. Price
W. C. Strahle
Atlanta, GA 30332

Massachusetts Institute of Technology
Department of Mechanical Engineering
ATTN: T. Toong
Cambridge, MA 02139

Pennsylvania State University
Applied Research Laboratory
ATTN: G. M. Faeth
P.O. Box 30
State College, PA 16801

Pennsylvania State University
Department of Mechanical Engineering
ATTN: K. Kuo
University Park, PA 16801

Princeton Combustion Research Laboratories
ATTN: M. Summerfield
N. Messina
1041 U.S. Highway One North
Princeton, NJ 08540

Princeton University
Forrestal Campus
ATTN: I. Glassman
F. Dryer
Technical Library
P.O. Box 710
Princeton, NJ 08540

Stevens Institute of Technology
Davidson Library
ATTN: R. McAlevy, III
Hoboken, NJ 07030

System Research Laboratory
ATTN: L. Goss
2600 Indian Ripple Rd.
Dayton, Ohio 45440

University of California
Dept. of Mechanical Eng.
ATTN: J. W. Daily
Berkeley, CA 94720

University of Florida
Dept. of Chemistry
ATTN: J. Winefordner
Gainesville, Florida 32601

University of Illinois
Dept. of Mechanical Eng.
ATTN: H. Krier
144 MEB, 1206 W. Green St.
Urbana, IL 61801

University of Utah
Dept. of Chemical Engineering
ATTN: A. Baer
Salt Lake City, UT 84112

NBS-114A (REV. 2-8C)

U.S. DEPT. OF COMM. BIBLIOGRAPHIC DATA SHEET (See instructions)	1. PUBLICATION OR REPORT NO. NBSIR 83-2689	2. Performing Organ. Report No.	3. Publication Date May 1983

4. TITLE AND SUBTITLE

Thermal Radiative Ignition of Liquid Fuels by a CO_2 Laser

5. AUTHOR(S)

Takashi Kashiwagi, Thomas J. Ohlemiller, Takao Kashiwagi and Walter W. Jones

6. PERFORMING ORGANIZATION (If joint or other than NBS, see instructions)

NATIONAL BUREAU OF STANDARDS
DEPARTMENT OF COMMERCE
WASHINGTON, D.C. 20234

7. Contract/Grant No.

AFOSR-ISSA-82-00014

8. Type of Report & Period Covered

Final progress report
Oct. 1, 1979-Sept. 30, 1982

9. SPONSORING ORGANIZATION NAME AND COMPLETE ADDRESS (Street, City, State, ZIP)

Air Force Office of Scientific Research
Building 410, Bolling Air Force Base
Washington, DC 20332

10. SUPPLEMENTARY NOTES

☐ Document describes a computer program; SF-185, FIPS Software Summary, is attached.

11. ABSTRACT (A 200-word or less factual summary of most significant information. If document includes a significant bibliography or literature survey, mention it here)

This report summarizes progress in the study of the ignition mechanism of a liquid fuel by a CW CO_2 laser; the period covered is from October 1, 1979 to September 30, 1982. It describes (1) new observations of liquid fuel behavior near and at the liquid/air interface during the laser irradiation with incident fluxes from 260 to 2500 W/cm^2, (2) new time-resolved measurements of distributions of temperature and vapor concentration in the gas phase using a newly-developed, high speed, two-wavelength holographic interferometer and (3) the development of a technique to measure infrared absorption spectra of fuel vapors at elevated temperatures.

12. KEY WORDS (Six to twelve entries; alphabetical order; capitalize only proper names; and separate key words by semicolons)

absorption; decanes; decenes; electromagnetic absorption; holographic interferometry; ignition; infrared radiation; vaporization

13. AVAILABILITY

☒ Unlimited

☐ For Official Distribution. Do Not Release to NTIS

☐ Order From Superintendent of Documents, U.S. Government Printing Office, Washington, D.C. 20402.

☒ Order From National Technical Information Service (NTIS), Springfield, VA. 22161

14. NO. OF PRINTED PAGES

84

15. Price

$11.50